Cartilage-targeting peptide-modified dual-drug delivery nanoplatform with NIR laser response for osteoarthritis therapy

Song Xue [a,1], Xiaojun Zhou [b,1], Weilin Sang [a,1], Cong Wang [a], Haiming Lu [a], Yiming Xu [a], Yiming Zhong [a], Libo Zhu [a,***], Chuanglong He [b,**], Jinzhong Ma [a,*]

[a] *Department of Orthopedics, Shanghai General Hospital, Shanghai Jiao Tong University School of Medicine, Shanghai, 200080, China*
[b] *State Key Laboratory for Modification of Chemical Fibers and Polymer Materials, College of Chemistry, Chemical Engineering and Biotechnology, Donghua University, Shanghai, 201620, China*

ABSTRACT

Cartilage-targeting delivery of therapeutic agents is still an effective strategy for osteoarthritis (OA) therapy. Recently, scavenging for reactive oxygen species (ROS) and activating autophagy have been increasingly reported to treat OA effectively. In this study, we designed, for the first time, a dual-drug delivery system based on metal organic framework (MOF)-decorated mesoporous polydopamine (MPDA) which composed of rapamycin (Rap) loaded into the mesopores and bilirubin (Br) loaded onto the shell of MOF. The collagen II-targeting peptide (WYRGRL) was then conjugated on the surface of above nanocarrier to develop a cartilage-targeting dual-drug delivery nanoplatform (RB@MPMW). Our results indicated the sequential release of two agents from RB@MPMW could be achieved via near-infrared (NIR) laser irritation. Briefly, the rapid release of Br from the MOF shell exhibited excellent ROS scavenging ability and anti-apoptosis effects, however responsively reduced autophagy activity, to a certain extent. Meanwhile, following the NIR irradiation, Rap was rapidly released from MPDA core and further enhanced autophagy activation and chondrocyte protection. RB@MPMW continuously phosphorylated AMPK and further rescued mitochondrial energy metabolism of chondrocytes following IL-1β stimulation via activating SIRT1-PGC-1α signaling pathway. Additionally, the cartilage-targeting property of peptide-modified nanocarrier could be monitored via Magnetic Resonance (MR) and IVIS imaging. More significantly, RB@MPMW effectively delayed cartilage degeneration in ACLT rat model. Overall, our findings indicated that the as-prepared dual-drug delivery nanoplatform exerted potent anti-inflammation and anti-apoptotic effects, rescued energy metabolism of chondrocytes *in vitro* and prevented cartilage degeneration *in vivo*, which thereby showed positive performance for OA therapy.

1. Introduction

Osteoarthritis (OA) is a ubiquitous cartilage degenerative disease, which have affected over 250 million people [1]. Despite with a high prevalence, the disease aetiology is still unclear and effective therapies are also limited so far [2]. Previous studies have indicated early intervention for cartilage degradation is effective in preventing OA progression, and several therapeutic drugs, such as nonsteroidal anti-inflammatory drugs (NSAIDs), have been commonly used to subjectively relieve the symptom [3,4]. However, these agents could not hinder OA progress fundamentally and might be implicated with certain side effects [4]. Therefore, exploring more new treatments that result in sound outcomes is a top priority for managing OA.

Generally speaking, considerably high level of oxidative stress is existed in the chondrocytes of OA, with numerous studies indicating the application of anti-oxidative agents holds great potential for OA treatment [5,6]. However, several free radical scavengers exhibit poor biocompatibility and potential cytotoxicity, which limits their further

---

applications [7,8]. Recently, bilirubin (Br), one of the products of bile acid metabolism, has been developed and found to have several biological functions including scavenging reactive oxygen species (ROS) [9–12]. However, to our best knowledge, its efficacy on OA treatment remains unknown. Based on some novel findings from Jon's group [13–16], we hypothesized that anti-ROS effect of bilirubin might also be utilized in OA treatment. To our excitement, our preliminary experimental results surely implied Br could rapidly eliminate ROS and rescue chondrocytes from overwhelming challenge of inflammatory cytokines, therefore it might hold great potential for OA therapy. However, Br was found to suppress the autophagy activity, to a certain extent, which might contribute to the potent inhibition of cellular ROS level reactively. This drawback might have side effects on chondrocytes for a long run.

There is no doubt that autophagy, a "self-eating" process, plays an important role in maintaining adaptive cellular response and homeostasis [17,18]. This process is different from cell apoptosis, in that it represents the programmed cell survival and has been implicated in the protective effects against OA development [17]. Rapamycin (Rap) which acknowledged to be one of mammalian target of rapamycin (m-TOR) inhibitor, is currently regarded as an activator of autophagy and a potent therapeutic agent in OA therapy [18]. For instance, Matsuzaki et al. found that Rap-incorporated gelatin hydrogels, which showed excellent controlled release manner, could exert protective effects on OA mice via intra-articular (IA) administration [19]. Encouraged by these results and to tackle with the shortcoming of Br, we attempted to combine it with Rap for realizing the complementary and synergetic protective effects for OA therapy.

Owing to the lack of blood vessels for cartilage, the drugs are hardly accessible to chondrocytes and exert protective effects [20]. Recently, models comprising IA injection of nanocarrier loaded with effective agents against OA have been developed prevailingly [21], which demonstrated to be a valid avenue realizing the controlled release manner and targeted therapy. Generally, this approach entails endogenous or exogenous stimulus responsive release of bioactive agents to its target and reduces systemic side effects [22–24]. Among various nanomaterials, polydopamine (PDA), which characterized with outstanding biocompatibility, biodegradation and adhesive properties, has attracted tremendous attention across various fields, including biosensor, bioimaging and drug delivery [25,26]. Several studies have also shown PDA possesses superior near-infrared (NIR)-responsive property, which makes them ideal candidate for application in multiple diseases theranostics [27,28]. To our excitement, NIR laser could efficiently penetrate into joint for arthritis therapy [29]. Meanwhile, PDA could act as a gatekeeper in controlling drug release by switching the NIR laser on and off. Previous report demonstrated that PDA-modified $Gd_2(CO_3)_3$ showed better solubility and acted as an excellent nanocarrier in OA therapy, meanwhile acting as a powerful gatekeeper [30].

Numerous studies have shown that mesoporous structure could enhance the drug-loading ability of PDA nanoparticles [31,32], and combining with other components was also found to boost the PDA versatility and synergistic performance for OA theranostics [33]. It's worth mentioning that numerous active bonds enable easy modification of mesoporous PDA (MPDA) [33,34]. For example, Yan et al. reported folic acid (FA) modified PDA carrier which further loaded with phthalocyanine-based photosensitizer exerted excellent tumor theranostics [35]. Another research demonstrated that hemoglobin (Hb) modified PDA (Hb-PDA) nanoparticles significantly enhanced the transportation of oxygen [34]. With these in mind, we have merged mesoporous PDA and metal organic framework (MOF) to generate a versatile nanocarrier, named MPM, to overcome the difficulty of effective drug delivery. Intriguingly, we also found there was a good MR imaging effect of MOF-decorated nanocarrier, which could further monitor the therapeutic effects *in vivo*.

Cartilage is mainly composed of dense type II collagen and proteoglycan, which results in the barrier of chondrocyte-targeted therapy. Several studies also demonstrated by targeting the component of

cartilage might provide an effective avenue for OA therapy [36,37]. Interestingly, it was reported WYRGRL, one of the collagen II-targeting peptides, led to about 72-fold increase of cartilage-targeting efficiency for the peptide-functionalized nanoplatform *in vivo* [38]. As for these, WYRGRL was further modified onto the surface of MOF in this study. It's worth mentioning dual-drug delivery system displayed NIR laser-triggered Rap-accelerated release manner owing to the component of PDA, which exerted complementary protective effect with Br. More significantly, this dual drug-loaded nanoplatform remarkably delayed cartilage degeneration in ACLT rat model, further demonstrating the superiority of RB@MPMW. Therefore, these results demonstrated as-prepared cartilage-targeted nanoplatform with NIR laser responsively promoting the sequential release of two agents could exert synergetic therapeutic effects on OA.

2. Methods

2.1. Reagents and materials

Dopamine hydrochloride (DA), tris (hydroxymethyl) aminomethane (Tris), iron (III) chloride hexahydrate ($FeCl_3 \cdot 6H_2O$), Pluronic® F127, Trimesic acid (H_3BTC), Cyanine 5 (Cy5) and Rhodamine B were provided by J&K Scientific (Beijing, China). Bilirubin and dimethyl sulfoxide (DMSO) were purchased from Sigma Aldrich (St. Louis, MO, USA). Rapamycin was obtained from Med Chem Express (Shanghai, China). WYRGRL was synthesized by ChinaPeptides (Shanghai, China). Cell culture reagents including fetal bovine serum (FBS), DMEM (High Glucose), antibiotics and trypsin-EDTA were purchased from Thermo Fisher Scientific (Scoresby, Vic, Australia). IL-1β was purchased from R&D Systems (Beverly, MA, USA). Cell counting kit 8 was provided by Dojindo (Tokyo, Japan). CYTO-ID® Autophagy detection reagent was purchased from ENZO Life Science (New York, USA). Lyso-Tracker Green, Hoechst 33342 and 4',6-diamidino-2-phenylindole (DAPI) dye were purchased from Beyotime (Shanghai, China). Antibodies against LC3B, Beclin-1, SQSTM1, P65, p-P65, Iκ-Bα, AMPK, p-AMPK, SIRT1 and PGC-1α were obtained from Cell Signaling Technology (Beverly, MA, USA). Anti-MMP9 antibody was purchased from Proteintech (Wuhan, China). Anti-β-Actin, anti-β-Tubulin and anti-GAPDH antibodies were purchased from Santa Cruz Biotechnologies (Santa Cruz, CA). ATDC5, a kind of mouse chondrogenic cell line, was obtained from Cell Bank of Biochemistry and Cell Biology, Chinese Academy of Science, China.

2.2. Synthesis of MPDA

Synthesis of mesoporous polydopamine (MPDA) was performed as previously reported with modified method [32]. Briefly, equal ratios (0.36 g each) of F127 and 1,3,5-trimethylbenzene (TMB) were evenly dissolved in a mixture of water (65 mL) and ethanol (60 mL), then exposed to ultrasonic conditions for 30 min. Thereafter, 90 mg of Tris was uniformly dissolved in 10 mL of water, mixed with the solution, then treated with ultrasound for 10 min. Dopamine (60 mg) was uniformly dissolved in 5 mL of deionized water, then added (dropwise) to the above solution. Finally, the mixed solution was stirred slowly at 300 xg for 4 h in darkness. The reaction system was then centrifuged at a high speed at 18590 xg for 1.5 h and the obtained product was dispersed in a mixture of ethanol (100 mL) and acetone (50 mL), followed by washing three times to remove the template. Finally, the resulting MPDA was dispersed in ethanol for further experiment.

2.3. Preparation of MPMW and fluorescence labeled MPMW

Summarily, 20 mg of the prepared MPDA was uniformly dispersed in 10 mL of deionized water, followed by dropwise addition of 10 mL $FeCl_3 \cdot 6H_2O$ (0.1 M) into the mixture. The mixture was stirred and incubated for 1 h at room temperature (RT). The products were collected through high-speed centrifugation (18590 xg, 15 min) and washed with

deionized water repeatedly, then uniformly dispersed into ethanol solution which predissolved with H_3BTC (0.1 M, 10 mL) following ultrasound treatment. The whole solution was stirred and incubated for half an hour in an oil bath environment set at 70 °C. Finally, the MOF-coated MPDA (MPM) were washed several times with ethanol and the self-assembly process was repeated three times to obtain the required MOF structure. Thereafter, MPM were uniformly dispersed in 15 mL of deionized water and activated by EDC (15 mg) and NHS (10 mg) for 2 h. After washed several times with deionized water, 3 mg of WYRGRL peptides were added into the solution. The mixture was then incubated at RT for 12 h. The peptides-conjugated MPM (MPMW) were obtained by high-speed centrifugation (18590 xg, 20 min), then washed with deionized water several times. The supernatant was also collected for detecting the content of peptides. To prepare Rhodamine B (RhB)-labeled MPMW or MPM (RhB-MPMW or RhB-MPM), 200 μL RhB solution (0.2 mg/mL) was added into the suspension of nanoparticles and stirred overnight. After the vacuum treatment and centrifugation, the RhB-MPMW or RhB-MPM were obtained. To synthesize the Cy5-labeled nanoparticles, Cy5 was firstly dissolved in DMSO and diluted with a concentration of 0.2 mg/mL. Then, 20 mg of MPM or MPMW was dispersed in deionized water (10 mL) via ultrasound, followed by addition of 200 μL Cy5 solution. The mixture was stirred in the dark overnight to obtain the Cy5-labeled MPM or MPMW (Cy5-MPM or Cy5-MPMW).

2.4. Characterization

The morphology of prepared MPDA, MPM and MPMW were observed using a Transmission Electron Microscope (TEM, JEM-2100), whereas size distribution was obtained via dynamic light scattering (DLS) test performed by a BI-200SM multiangle dynamic/static laser scattering instrument (Brookhaven, USA). The X-ray diffraction (XRD) patterns were obtained by D/max-2550VB+/PC diffractometer (RIGAKU, Japan) with CuKα radiation at 2θ angle of 5–40°.

2.5. Photothermal effect determination

To systemically evaluate the photothermal effect of MPMW, we performed *in vivo* and *in vitro* assays. Firstly, the MPMW were dispersed in PBS (100 μg/mL) and put into Eppendorf tubes, then irradiated with NIR laser at 808 nm (1 W/cm^2) for 600 s. Photothermal behavior *in vivo* was also determined using the method above. Briefly, 4-week-old Sprague Dawley (SD) rats were obtained from Slac Laboratory Animal Co. Ltd. (Shanghai, China). After anesthetization, 20 μL MPMW (100 μg/mL) and PBS were injected into the rat right knee joint, respectively, and the NIR laser (808 nm, 1 W/cm^2) were irradiated just on the rat right knee joint for 600 s at 12 h after injection. The infrared camera was utilized to collect the images and corresponding temperature variation during the laser irradiation. PBS was set as the control *in vivo* or *in vitro*.

2.6. Drug loading and release

Briefly, after removal of the template, the pores of MPDA were exposed. 20 mg of MPDA was weighed and dispersed in water, followed by addition of 5 mg of Rap. The mixture was stirred overnight at RT under darkness. Rap was further absorbed into the pores by vacuum treatment, and then the supernatant was collected following high-speed centrifugation as described above and washed for further detection. After MOF layers were coated onto the Rap-loaded MPDA, 5 mL Br solution (1 mg/mL) was added and then stirred overnight under darkness. Finally, the resulting Rap and Br-loaded MPM (RB@MPM) was subjected to vacuum treatment, high-speed centrifugation and washing. We collected the supernatant to perform high performance liquid chromatograph (HPLC) analysis with the thermo-C18 analytical column according to previous studies [39,40]. The results were further quantified based on the similar method reported previously [41]:

Encapsulation ratio (ER) = (weight of the drug encapsulated in nanoparticles)/(weight of the total feeding drug) × 100%.

Owing to the pH value of synovia from arthritis could be as low as 6.0, the drug release was studied at both pH 7.4 and pH 6.0 [37]. The drug release from RB@MPMW at two different pH (7.4 or 6.0) or different temperature (37 or 45 °C) were investigated. Summarily, 5 mg of drug-loaded particles were dissolved in 1 mL of PBS at different conditions (pH = 7.4, 37 °C; pH = 6.0, 37 °C and pH = 6.0, 45 °C), placed into an analysis bag and then immersed into the corresponding PBS (9 mL). 5 mL of soaking solution was extracted at an indicated time points and replaced with 5 mL of fresh PBS. The resultant supernatants were eventually collected for HPLC detection. In addition, the influence of NIR laser at different pH condition on drug release efficiency was also explored. As for determination of cumulative release of Br, 5 mg of RB@MPMW suspended in PBS (1 mL) at different pH (6.0 or 7.4), which placed into analysis bag and then immersed into the corresponding PBS (9 mL). At indicated time points, the suspensions were vertically irradiated with NIR laser (808 nm, 1 W/cm^2) for 10 min. Finally, the supernatants before and after laser irradiation were subjected for further detection. As for assessing the cumulative release percent of Rap, according to our preliminary results above, the cumulative release of Rap in the first 24 h was limited owing to the MOF shell affecting its release efficiency. After incubation for 24 h at different pH (6.0 or 7.4), the different samples were subjected to NIR laser irradiation at indicated time points and the other detective method was similar to that of Br. These experiments above were carried out in triplicates.

2.7. In vitro cytotoxicity assay

Cytotoxicity of MPMW and RB@MPMW against ATDC5 cells was evaluated using CCK-8. Specifically, ATDC5 cells were adhered to the bottom of 96-well plates at a density of 5×10^3 cells per well. The two nanoparticles were suspended in culture medium at different concentrations (0, 6.25, 12.5, 25, 50, 100, 200 and 400 μg/mL) and the cells were incubated with the culture medium above for 24 and 72 h, respectively. During the incubation time, the ATDC5 cells was irradiated under NIR laser (808 nm, 1 W/cm^2) for 10 min every 12 h. Thereafter, the cells were incubated with 10% CCK-8 solution for 2 h according to manufacturer's protocol, followed by determination of absorbance at 450 nm using a microplate reader (Spectra Max, Molecular Devices, USA).

2.8. In vitro and ex vivo cellular uptake assays

To analyze the cellular uptake efficiency of nanoparticles, we performed bio-TEM, confocal laser scanning microscopy (CLSM) scanning and flow cytometry detections. Efficiency of cellular uptake was visualized by CLSM. ATDC5 cells were firstly attached onto glass coverslips, and then different concentrations of RhB-MPMW (0, 25, 50 and 100 μg/mL) were added into the cell supernatant and incubated for 4 h. The mixture was then washed with PBS three times and fixed using 4% paraformaldehyde (PFA) solution for 30 min. Thereafter, the cells were permeabilized using 0.1% Triton X-100 solution for 15 min and subsequently incubated with DAPI for 5 min. Finally, the samples were subjected to CLSM for detection.

Moreover, we conducted ex vivo assay to explore the cartilage-targeting efficiency. Six femoral heads from SD rats were successfully removed from three normal six-week-old rats, washed three times in PBS and then randomly divided into two groups (three samples per group): 1) DMEM (High Glucose) complete culture medium containing 50 μg/mL RhB-MPM; 2) DMEM (High Glucose) complete culture medium containing 50 μg/mL RhB-MPMW. These samples were co-cultivated with complete culture medium for two days, then subjected to fabrication of histologic sections and further tissue fluorescence detection.

2.9. Intracellular ROS levels determination

Intracellular ROS levels were measured using a Reactive Oxygen Species Assay Kit (DCFH-DA, Beyotime, China). In order to simulate the aseptic inflammatory pathological process of chondrocytes *in vitro*, we use IL-1β (10 ng/mL) as a stimulation factor. Briefly, ATDC5 cells were seeded into six-well plates, incubated with various nanoparticles (50 μg/mL) for 4 h, then stimulated with IL-1β (10 ng/mL) for 72 h. During the period, ATDC5 cells were exposed to NIR laser for 10 min every 12 h as described above. After treatment, the cells were incubated with DCFH-DA working solution for 20 min, washed three times with PBS and then subjected to fluorescence detection.

2.10. TUNEL staining

To analyze the anti-apoptosis effect of different nanoparticles, we performed a terminal deoxynucleotidyl transferase-mediated dUTP-biotin nicked labeling (TUNEL) assay. ATDC5 cells were pre-treated with samples (50 μg/mL) for 4 h and then IL-1β (10 ng/mL) was separately added into the supernatant of corresponding groups, followed by a 10-min exposure to NIR laser every 12 h (808 nm, 1 W/cm^2). After incubation for 72 h, ATDC5 cells were washed with PBS three times, fixed with 4% PFA for 20 min, then punched with 0.1% Triton X-100 for 15 min. Finally, the samples were stained with TUNEL assay kit (Yeasen, Shanghai, China) according to the manufacturer's instructions.

2.11. Quantitative real-time PCR

ATDC5 cells were pre-treated with various nanoparticles (50 μg/mL) for 4 h and then exposed to IL-1β (10 ng/mL) for 36 h or 72 h. During the incubation time, the cells were exposed to the NIR laser (808 nm, 1 W/cm^2) for 10 min every 12 h. Total RNA was then isolated from each group according to our previous study [42]. The RNA was reverse-transcribed and subjected to quantitative real-time PCR (qRT-PCR) using the SYBR® Premix Dimer Eraser™ (TaKaRa, Japan). Primers identity and corresponding sequences were showed in Table S1. The genes expression of TNF-α, IL-6, MMP9, ADAMTS5, Aggrecan and Col2a1 were calculated via $2^{-\triangle\triangle CT}$ method, and β-Actin was used as a reference gene.

2.12. Western blot analysis

The sample preparation process was similar with the procedure for RNA isolation mentioned above. After incubation for 36 or 72 h, the cells were lysed in ice-cold RIPA containing protease inhibitor cocktail (Sigma-Aldrich, USA) for 30 min. The lysates were then centrifuged at 12000 rpm for 20 min at 4 °C and the supernatant was collected. Protein concentration was quantified using a BCA protein assay kit (Beyotime, China) according to manufacturer's protocol. Then equal concentration for each sample was loaded and separated by SDS-PAGE. The proteins were transferred to polyvinylidene difluoride (PVDF) membranes (Millipore, Billerica, MA, USA), blocked in 5% non-fat milk for 1 h at RT and then incubated with primary antibodies at 4 °C overnight. Thereafter, the mixture was conjugated by peroxidase secondary antibody for 1 h. Finally, immunoreactive proteins were detected using an enhanced chemiluminescence kit (Millipore, USA) according to manufacturer's instructions.

2.13. Seahorse metabolic analysis

After ATDC5 cells were seeded into 96-well plates, different groups pre-incubated with different samples (50 μg/mL, 4 h) were exposed to IL-1β (10 ng/mL) for 24 h. During the incubation period, the cells were also exposed to NIR laser for 10 min every 12 h as described above. Cellular oxygen consumption rate (OCR) was analyzed using the XF-96 Flux Analyzer (Seahorse Bioscience). Specifically, ATP production from each group was first measured by treating chondrocytes with ATP synthase inhibitor, oligomycin (1.5 μM). Then FCCP (1.5 μM) was added into the supernatant, and the increase of oxygen consumption was also detected as the maximum oxygen consumption capacity of mitochondria, which indirectly indicated the maximum mitochondrial respiration ability. Antimycin A and retenone (1.25 μM), which inhibited the respiratory chain and completely suppressed oxygen consumption in mitochondria, were further added into the supernatant as the last step. The main parameter values were determined according to previous research [43].

2.14. Establishment and treatment of the anterior cruciate ligament transection (ACLT) rat model

This experiment was approved by the Research Ethics Committee of Shanghai General Hospital (#2019AWS0008). Summarily, 25 4-week-old SD rats were purchased from Slac Laboratory Animal Co. Ltd. and divided into five groups (n = 5). Twenty of them were subjected to ACLT surgery according to our previous research [44,45]. Specifically, rats were first anesthetized using an intraperitoneal injection of chloral hydrate (10%, 300 μL/100 g), then the right knee joint skin and joint capsule were opened to fully expose the joint cavity. The cruciate ligament was carefully transected using a scalpel. Thereafter, the right joint capsule and its surrounding skin were completely sutured. Finally, the ACLT model was confirmed using an anterior drawer test. Different groups were treated as follows: 1) Sham group: rats didn't undergo ACLT surgery or treatment; 2) ACLT group: OA rats IA injected with 20 μL PBS; 3) Rap@MPMW group: OA rats IA injected with 20 μL Rap@MPMW (50 μg/mL); 4) Br@MPMW group: OA rats IA injected with 20 μL Br@MPMW (50 μg/mL) and 5) RB@MPMW group: OA mice IA injected with 20 μL RB@MPMW (50 μg/mL). The sample injection was performed every four days for six weeks. After injection for 12 h, the right knee joint was exposed to local photothermal radiation (808 nm, 1 W/cm^2) for 10 min. All rats were normally housed in the Animal Center of Shanghai General Hospital. Before sacrificed, the blood samples were obtained from the retro orbital veins of rats in different groups, and each blood sample was subjected to analysis of blood cell by analyzer Sysmex XT-2000i (Sysmex Corporation, Japan) and determination of some biochemical indexes in serum via HITACHI 7180 Automatic Biochemical Analyzer (HITACHI Corporation, Japan). All rats were finally sacrificed for further histological evaluation.

2.15. Determination of relaxation time and MR imaging in vitro and in vivo

MPM and MPMW nanoparticles were suspended in PBS at different Fe concentrations (0.025, 0.05, 0.1, 0.2 and 0.4 mM). *In vitro*, the T1 relaxivity (r1) of each sample was determined by scanning under 0.5 T NMI20-Analyst NMR Analyzing and Imaging system (Shanghai, China). As for *in vivo* assay, the ACLT rats were first anesthetized, then MPM and MPMW solutions (50 μg/mL, 20 μL) were thereafter injected into the ACLT rats model intra-articularly, respectively. Then the rats were fixed in the center of the head coil and scanned using a 7.0 T Micro-MRI scanner (Bruker, PharmaScan, USA) with an aperture of 16 cm and a maximum gradient intensity of 300 mT/m. Finally, T1-weighted MR images of the two samples were collected at predetermined times.

2.16. IVIS imaging

In order to detect the cartilage-targeting effect of different samples, we performed IVIS imaging determination. Briefly, Cy5-MPMW and Cy5-MPM (50 μg/mL, 20 μL) were intra-articularly injected into ACLT rats, then the rats were scanned under IVIS Spectrum Imaging System (Lumina Series, USA). These IVIS images were collected for several days with the excitation and emission wavelength at 675 and 695 nm, respectively. Furthermore, the distribution for each sample in the knee

joint as well as other important organs were also analyzed via IVIS scanning.

2.17. Histopathological and immunohistochemical analysis

After six weeks of treatment, all rats were sacrificed and their right knee joints were harvested. These samples were fixed in 4% PFA and decalcified in 10% EDTA, then embedded in paraffin. Sagittal section of the specimen was cut into 4 μm-thick sections respectively, then stained with hematoxylin and eosin (H&E), Safranin O/Fast green (S/F). Their Osteoarthritis Research Society International (OARSI) scores were semi-quantitatively determined according to our previous report [44]. In addition, we performed immunohistochemical staining for detection of protein expression, including P65, MMP9 and LC3B.

After the sections were deparaffinized and hydrated, 3% hydrogen peroxide was used to reduce endogenous oxidation, and proteinase K was used for enzymatic repair of the tissue sections. After washed with PBS for three times, the sections were blocked with 1% BSA for 15min. We then incubated the samples with different antibodies overnight at 4 °C, including LC3B (#43566, dilution 1:400), P65 (#8242, dilution 1:400) and MMP9 (#10375-2-AP, dilution 1:300). After that, we used a DAB Kit (BD Biosciences, San Jose, CA, USA) to perform the secondary antibody incubation. Furthermore, some functional data of rats and some key organs, including the heart, spleen, lung, liver and kidney, were collected from individuals across various groups and used to assess systemic side effects of these nanoparticles.

2.18. Statistical analysis

All statistical analyses were performed using SPSS 22.0 software (IBM Corporation, USA) and all data were presented as means ± standard deviations (SD) for at least three independent experiments. Student's t-test or one-way analysis of variance (ANOVA) was used to compare the differences between various treatment groups (*, # indicate $p < 0.05$; **, ## indicate $p < 0.01$; ***, ### indicate $p < 0.001$; ns indicates not significant).

3. Results

3.1. Characterizations of as-prepared nanoparticles

Firstly, RB@MPMW nanoparticles were successfully synthesized as schematically illustrated in Fig. 1A. A clear mesoporous structure was observed on the surface of prepared MPDA which displayed the particle size of approximately 40 nm. However, after construction of the MOF structure, a clear boundary appeared on the surface. We could also find there was no significant difference between MPM and MPMW (Fig. 1B). DLS results showed that MPDA had a hydrodynamic diameter of about 89.7 nm, however the hydrodynamic diameter increased to 114.1 nm following the construction of MOF layer (Fig. 1C). Although the particle size was larger than that of TEM observation, this result was reasonable according to the previous theory [46].

Further, infrared spectra result showed the different components of drug-loaded system during preparation (Fig. S1A-D). As illustrated in Fig. S1B, after preparation of MOF structure, it showed a special
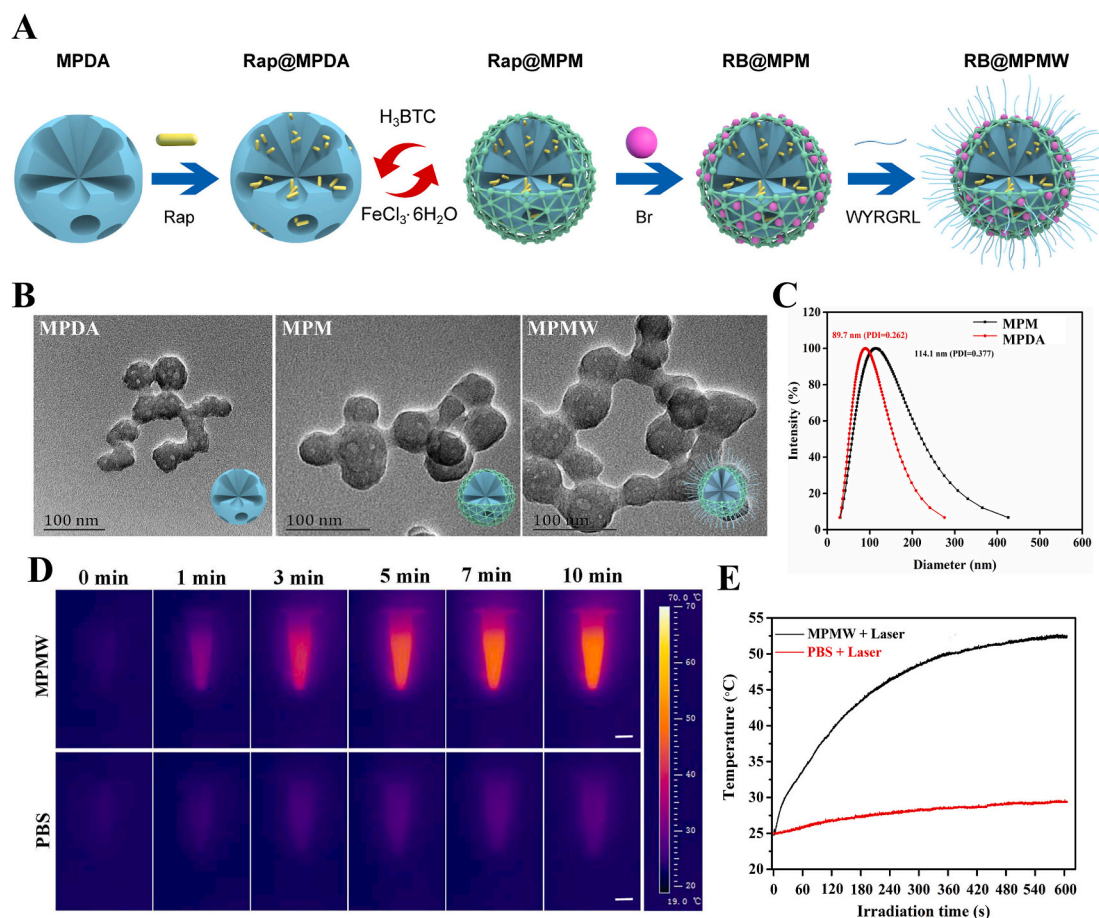
Fig. 1. (A) The schematic diagram of fabrication of RB@MPMW. (B) TEM images of MPDA, MPM and MPMW, respectively. (C) DLS of MPDA & MPM in deionized water. (D) Photothermal performance of MPMW (100 μg/mL) in aqueous solution under NIR irradiation (808 nm, 1 W/cm²) at different time points (scale bar: 0.3 cm). (E) The temperature changes at indicated time *in vitro* with or without MPMW.

absorption peak at 1710 cm^{-1}, which belonged to the carboxyl structure of H$_3$BTC. In the infrared spectrum of RB@MPMW, the special peak of carboxyl in H$_3$BTC was disappeared, however, a new special peak appeared at about 1698 cm^{-1}, which belonged to the amide bond formed after the reaction of WYRGRL with the carboxyl of H$_3$BTC, thus proving the successful modification with collagen II-targeting peptide. The absorption peak at 1685 cm^{-1} was from the carboxyl in Br. At the same time, Br and RB@MPMW had a strong absorption peak at about 3400 cm^{-1} as showed in Fig. S1C, which came from the N–H bond in pyrrole ring [10] and proved the successful loading of Br into the carrier. What's more, Rap and RB@MPMW had strong absorption peak at about 993 cm^{-1}, which was the bending vibration peak of C–H connected to C≡C in Rap [47], further proving Rap successfully loaded into these nanocarriers (Fig. S1D). The nitrogen adsorption–desorption isotherms revealed the presence of a hysteresis ring, indicating the existence of mesopores on the surface of nanoparticles. We also found that MPDA had a pore size of about 3.36 nm and a surface area of about 204.31 m^2/g (Fig. S2A). After construction of MOF structure, larger mesopores (5.17 nm) on the surface were observed and its surface area increased to 467.07 m^2/g. Additionally, the XRD result showed that a more obvious

characteristic peak was appeared in MPM as compared with MPDA, suggesting the successful coating of MOF (Fig. S2B).

The surface potential of various nanoparticles changed significantly. As shown in Fig. S2C, the surface charge of bare MPDA was found to be −7.1 mV, whereas the MOF-coated MPDA was positive charged, possibly due to abundance of Fe^{3+} in MOF. However, this potential slightly dropped following the peptide modification. Interestingly, the mapping diagram revealed different patterns of distribution across various elements in MPM, including O, N, C and Fe (Fig. S2D).

3.2. Photothermal imaging property

Owing to the component of MPDA, the photothermal property of the nanocarrier and NIR laser-accelerated drug release manner were endowed (Fig. S3A). Firstly, we conducted the impact of different power density on the viability of ATDC5 cells, the result showed there was no significant impact of NIR laser on the viability of ATDC5 cells when the laser power density was up to 1.0 W/cm^2 (Fig. S3B). According to previous studies, NIR irradiation at 1 W/cm^2 (808 nm) intermittently does not damage the cartilage and surrounding tissues *in vivo* [23,29]. Zhao
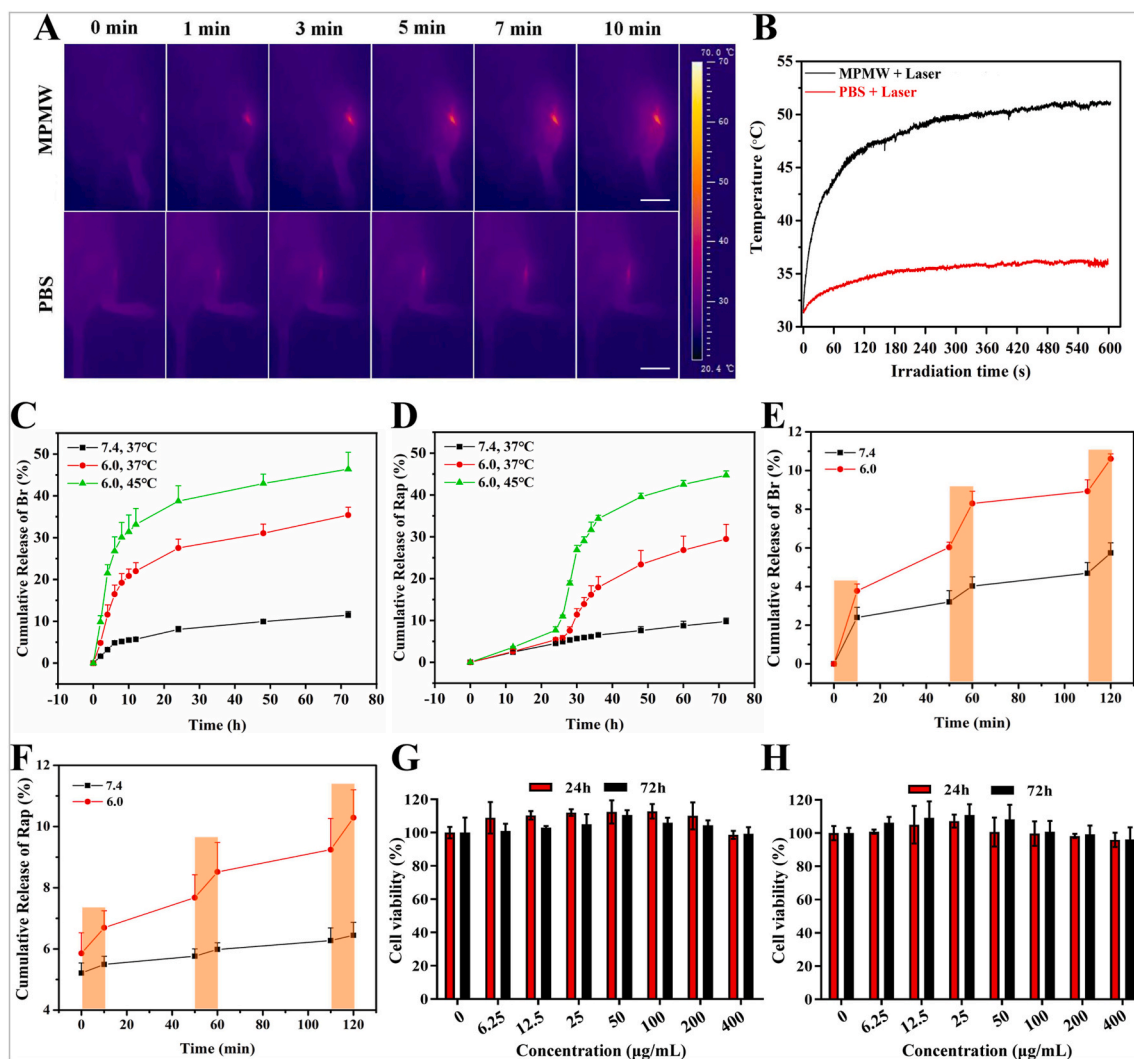
Fig. 2. (A) Photothermal performance of MPMW (100 μg/mL) in the knee joint under NIR laser irradiation (808 nm, 1 W/cm^2) at different time points (scale bar: 2 cm). (B) The temperature changes at indicated time *in vivo* with or without MPMW. (C,D) The cumulative release of Br and Rap from the BR@MPMW at different pH (7.4 or 6.0) and temperature (37 °C or 45 °C), respectively. (E,F) NIR laser-triggered release of dual agents under NIR laser irradiation at different pH (7.4 or 6.0) and different time points. The cumulative release of Rap was start to assessed after incubation for 24 h at indicated conditions. (G,H) Cell viability assay of ATDC5 cells incubated with (G) MPMW and (H) RB@MPMW at different concentrations (0, 6.25, 12.5, 25, 50, 100, 200 and 400 μg/mL) under NIR laser irridation for 10 min every 12 h.

et al. also demonstrated that MoS$_2$@CS@Dex NPs irradiated by NIR (1 W/cm^2) intermittently exhibited excellent therapeutic effect for OA with low cytotoxicity *in vitro* and systemic toxicity *in vivo* [24]. Therefore, we chose this density for subsequent studies. As shown in Fig. 1D, the photothermal signal intensity in MPMW group exhibited a gradual increase manner after irradiation for 10 min *in vitro*, with the temperature alteration of 28 °C (Fig. 1E). However, only an increase of 3 °C was detected for PBS group after NIR irradiation. Dynamic photothermal imaging and temperature alteration *in vivo* were also recorded in detail as illustrated in Fig. 2A and B. Based on the results above, we could easily conclude that there was a significant photothermal effect compared to PBS group.

3.3. In vitro dual-drug release

The cumulative release of dual drugs from RB@MPMW under different pH and temperature were determined via HPLC. First of all, based on the formula, the encapsulation ratios of the two agents were as follows: ER$_{Br}$ = 8.9%; ER$_{Rap}$ = 5.6%. According to the ICP results in Fig. S4A, we could find that acidic environment (pH 6.0) could accelerate the collapse of the MOF shell, which was in accordance with reported studies [48–50].

As revealed in Fig. 2C and D, only 8.01% and 11.38% of Br were released in the first 24 h and 72 h at the condition of 37 °C and pH 7.4. However, there were 38.74% and 46.38% of Br diffusing out at the same time at 45 °C and pH 6.0. Different from the release manner of Br, the cumulative release of Rap in the first 24 h was limited under three different conditions, which contributing to the MOF shell affecting the release of Rap. However, with the collapse of MOF shell, the blocking effect on Rap was gradually removed. After 24 h, there was a significant increasing release manner at 45 °C and pH 6.0, whereas it was clear that about 44.7% of Rap diffusing out at 72 h.

Additionally, the impact of NIR laser on drug release was also investigated. As illustrated in Fig. 2E and F, it was clear that NIR laser irritation significantly accelerated release of Br and Rap in a pH-dependent manner. At pH 6.0 and after NIR laser irritation, about 10.29% of Rap and 10.61% of Br released out in the first 2 h, whereas only 6.45% of Rap and 5.74% Br released out at the same time as for a neutral pH condition.

3.4. Cytotoxicity and hemolysis evaluation of nanoparticles

Cytotoxicity of MPMW and RB@MPMW against ATDC5 cells under NIR laser irridation (10 min per 12 h) were assessed using CCK-8 assay at different concentrations (0, 6.5 12.5, 25, 50, 100, 200 and 400 μg/mL). As showed in Fig. 2G and H, there was no obvious cytotoxicity for the concentrations of these two nanoparticles ranging from 6.25 to 400 μg/mL following one or three days of exposure. We also conducted hemolysis assay and live-dead cell staining analysis, these results showed in Fig. S3C-F further indicating there is no obvious cytotoxicity of MPMW or RB@MPMW as for the concentration up to 400 μg/mL, further indicating their favorable biocompatibility.

3.5. Cellular internalization of nanoparticles in vitro and ex vivo

Efficient uptake could facilitate the loaded agents to be delivered into the cells and then exert pharmacological effects. We firstly assessed cellular uptake of MPMW *in vitro* by bio-TEM observation. From the bio-TEM images, many nanoparticles were internalized by ATDC5 cells. It also could be seen that the cellular uptake of nanoparticles was increased as the particle concentration increased from 25 to 50 μg/mL (Fig. S4B and C). The cellular internalization of nanocarriers was further evaluated using different concentrations of RhB-MPMW and RhB-MPM (0, 25, 50 and 100 μg/mL) by CLSM observation. After the nanoparticles were incubated with ATDC5 cells for 4 h, the cellular uptake could be determined from the fluorescent images. It could be seen that

the red fluorescence intensities were increased with the increasing particle concentration, and there was no significant difference between the uptake efficiency of these two kind of nanoparticles (Fig. 3A and Fig. S4D). Notably, the nanoparticles were internalized in the cytoplasm of ATDC5 cells and distributed around the cell nuclei, which was obviously observed at the particle concentration of 100 μg/mL. Flow cytometry was also utilized to detected the cellular uptake efficiency *in vitro*. After incubation with RhB-MPMW (0, 50 and 100 μg/mL) for 4 h, we found the mean fluorescence intensity was elevated with the increased particle concentrations (Fig. S4E-H), similar with the results obtained from CLSM images, which further verified the above experimental results.

In contrast with the cellular uptake detection *in vitro*, the uptake of nanoparticles by cartilage tissues encountered many challenges. Cartilage is composed of a dense meshwork of type II collagen, making it a barrier for drug penetration. Nevertheless, we tried to assess whether RhB-MPMW had good cartilage affinity and penetrative ability using an ex vivo assay. After 48 h pretreatment with RhB-MPMW and RhB-MPM, histochemical fluorescence images of articular cartilage revealed a stronger fluorescence intensity in the RhB-MPMW group (Fig. 3B), indicating that peptides grafting could enhance the chondrocyte-targeting effect in the cartilage effectively. Taken together, these findings indicated that MPMW could be endocytosed by chondrocytes *in vitro* and specifically target cartilage.

3.6. Scavenging for ROS and anti-apoptosis effects evaluation

ROS are free radicals mainly generated from mitochondria, with excessive production implicated in damaging the normal cell microstructure and cellular functions [51]. In addition, excessive ROS may lead to senescence and apoptosis of chondrocytes [52]. Previous studies have shown that IL-1β is a classical cytokine that initiates a strong inflammatory response and increases production of cellular ROS level. We therefore pretreated ATDC5 cells with different samples (50 μg/mL) for 4 h, then exposed them to IL-1β (10 ng/mL) for 72 h. After treatment, DCFH-DA was applied to specifically detect the ROS levels for different groups. These groups showed different ROS scavenging abilities (Fig. 4A). The Rap@MPMW treatment showed reduced level of ROS in chondrocytes. In the Br@MPMW treated group, there was a more significant reduction in ROS level compared with the control and Rap@MPMW groups. By contrast, RB@MPMW group presented the strongest anti-ROS effect. These findings confirmed that Br-loaded nanoparticles exerted remarkable anti-oxidative stress effect, which was consistent with the findings by Jon's group [12,15].

Next, TUNEL staining assay was performed to comprehensively explore the anti-apoptotic effects of different samples. It was found that IL-β (10 ng/mL) treatment significantly increased the percentage of apoptotic cells (Fig. 4B). However, treatment with Rap@MPMW, Br@MPMW and RB@MPMW resulted in a significant decrease in the rate of apoptotic cells, especially the dual-drug loaded sample, which synergistically attenuated cellular inflammatory senescence and apoptosis (Fig. 4C and D). Collectively, these results indicated dual-drug delivery system successfully attenuated ROS production as well as the incidence of apoptosis in inflammatory microenvironment *in vitro*. Furthermore, it was worth mentioning that Br had more powerful protective effects against inflammation than Rap in chondrocytes.

3.7. OA-related genes expression determination

Numerous studies have implicated various genes in the pathological progression of OA. During the early stage of OA, chondrocytes reactively secreted some proinflammatory cytokines and chemokines [53]. Consequently, cumulative inflammatory factors, such as TNF-α and IL-6, activated inflammatory-related signaling pathways in chondrocytes [54]. Generally speaking, the cartilage extracellular matrix (ECM) mainly comprises type II collagen and aggrecan and can be degraded by
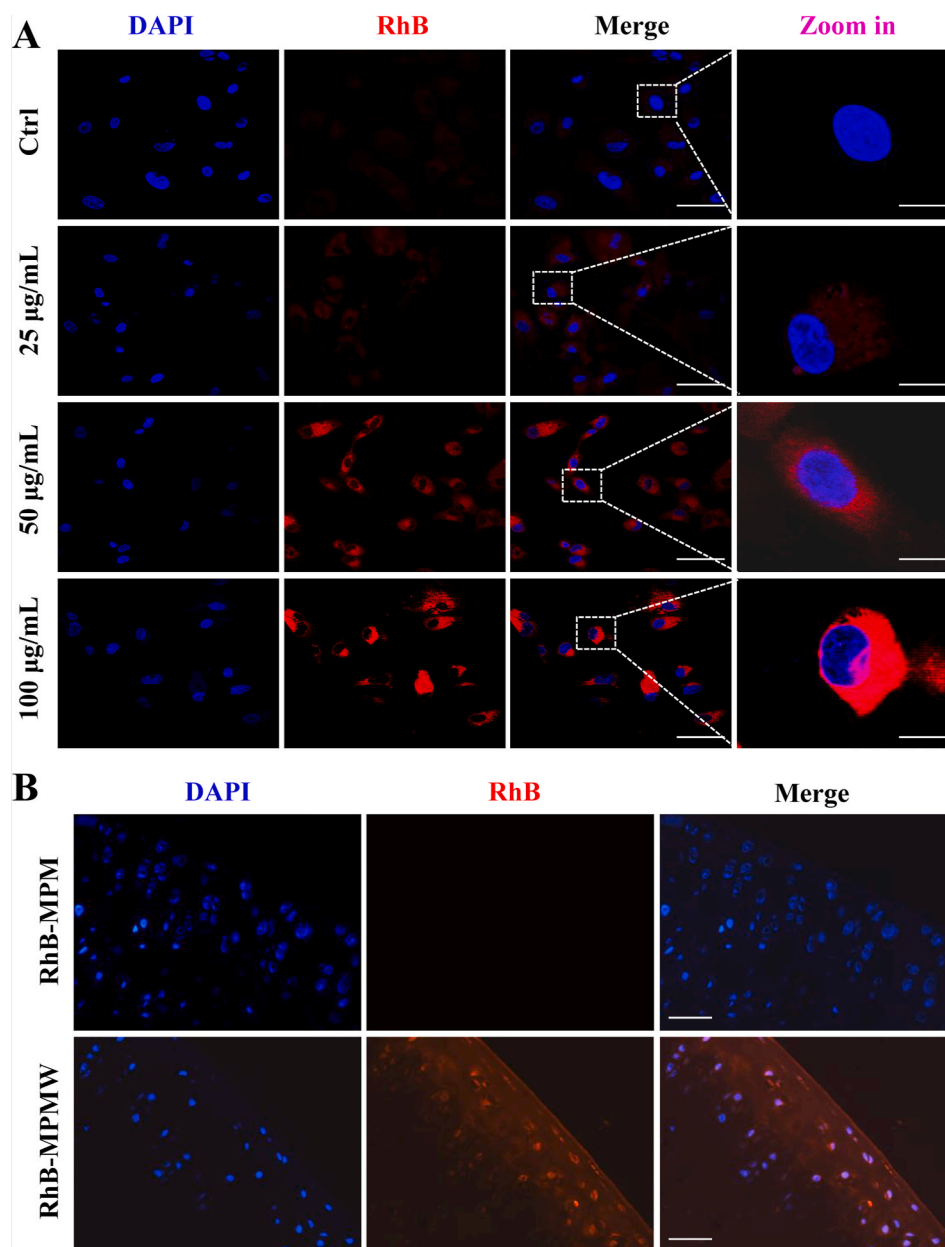
Fig. 3. (A) CLSM images of ATDC5 cells incubated with different concentrations of RhB-MPMW for 4 h (scale bar: 45 μm (before zoom in); 15 μm (after zoom in)). (B) The histological fluorescence images of articular cartilage pretreated with RhB-MPM (upper) & RhB-MPMW (lower) for two days (scale bar: 45 μm).

proteases such as MMP9 and ADAMTS5 during the progression stage of OA [55]. These inflammatory factors and proteases are also reportedly overexpressed in the inflammatory microenvironment. Thus, qRT-PCR analysis was performed to determine whether drug-loaded nano-carriers exerting protective effects on the catabolism and inflammatory response of chondrocytes after IL-1β treatment. As shown in Fig. 5A, a significant upregulation of TNF-α, IL-6, MMP9 and ADAMTS5 was observed after IL-1β treatment alone, whereas the mRNA expressions of Aggrecan and Col2a1 were significantly downregulated. With the addition of Rap@MPMW, Br@MPMW and RB@MPMW, the mRNA expressions of TNF-α, IL-6, MMP9 and ADAMTS were significantly downregulated, while the expressions of Aggrecan and Col2a1 were found to be gradually upregulated. Similarly, after treated for three days, the RB@MPMW-treated group showed more prominent anti-inflammation and anti-catabolism ability in chondrocytes than Rap@MPMW and Br@MPMW, implying the splendid synergistic effect of Rap and Br for OA therapy. (Fig. 5B). Overall, RB@MPMW possessed

the biological function of effectively suppressing the catabolism and inflammatory response of chondrocytes in the inflammatory microenvironment.

3.8. Effects of dual-drug nanocarrier on autophagy and the NF-κB signal pathway

As shown in Fig. 6A, the NF-κB signaling pathway has been considered as a key regulatory pathway for initiation and development of inflammation response. In addition, P65 has been reported to play a key role in this signaling pathway. Briefly, phosphorylation of P65 (p-P65), followed by its migration into the nucleus, makes it acting as a key transcriptional regulator, thereby initiating the transcription of various inflammatory factors, chemokines and matrix metalloproteinases. In this study, p-P65 was upregulated at two time points following IL-1β treatment, which also demonstrated the effectiveness of IL-1β-induced inflammation model *in vitro* (Fig. 6A and S4I). However, treatment with
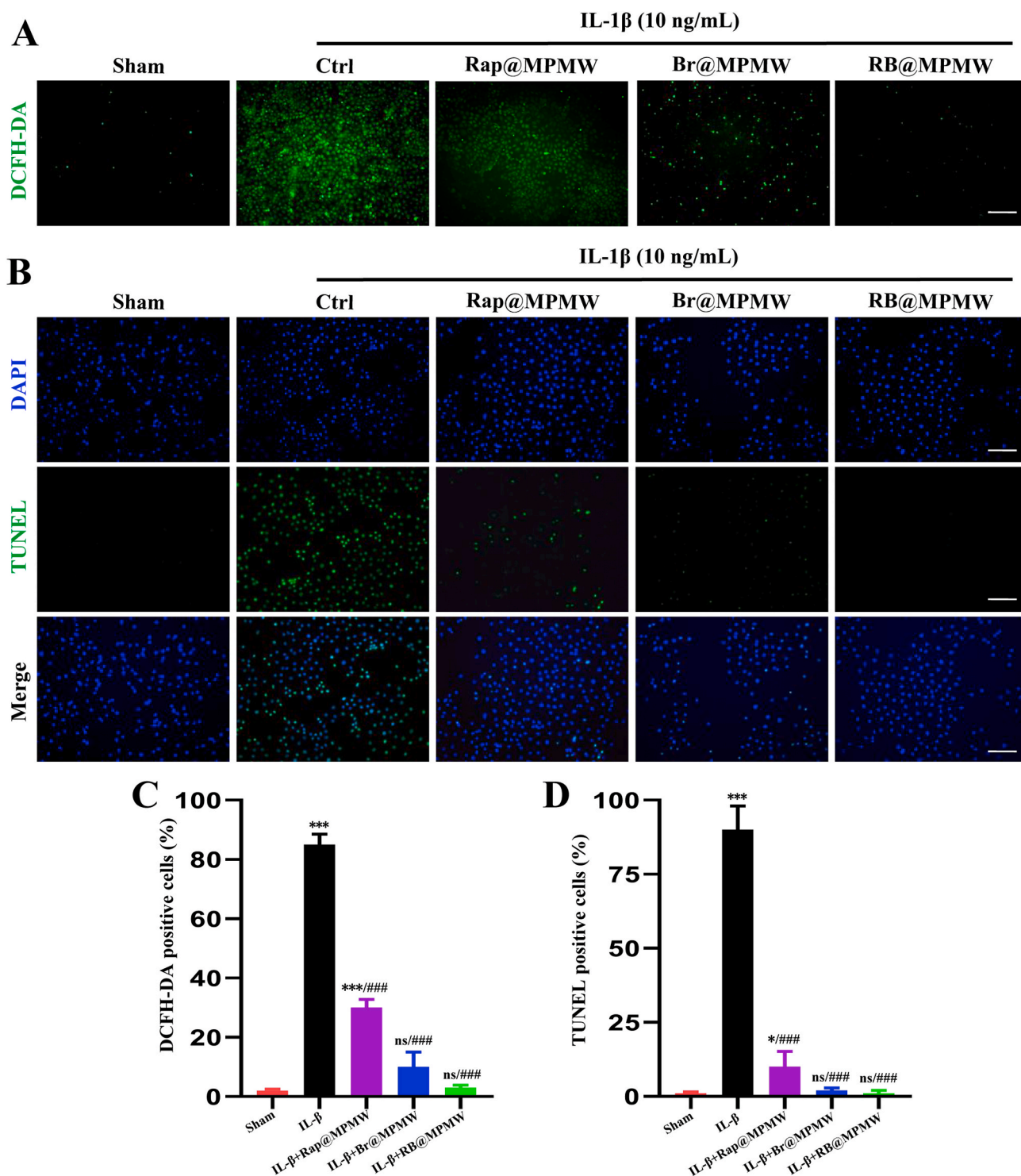
Fig. 4. (A) ROS measurement of ATDC5 cells after different samples treatment and subsequent IL-1β (10 ng/mL) stimulation for 72 h (scale bar: 45 μm). (B) Anti-apoptotic effects on ATDC5 cells of different samples after stimulation with IL-1β (10 ng/mL) for 72 h (scale bar: 45 μm). (C,D) The percent of DCFH-DA positive cells and TUNEL positive cells, respectively. * indicates p < 0.05; ***, ### indicate p < 0.001; ns indicates not significant. * indicates comparisons with the sham group and # indicates comparisons with the IL-1β treatment group.

drug-loaded samples significantly suppressed p-P65 expression in different degree, suggesting the successful suppression of NF-κB signaling pathway.

We then used the ratio of LC3 II/GAPDH revealing autophagy rather than the LC3B II/I ratio, owing to the high sensitivity of LC3B II in western blot analysis [56]. Following the treatment with IL-1β for 36 or 72 h (Fig. 6A and S4J), the LC3 II/GAPDH ratio and Beclin-1 were

further significantly downregulated. P62/SQSTM1, a substrate of auto-lysosome, revealed an opposite expression pattern to LC3B II/GAPDH ratio and Beclin-1 at these two time points. Summarily, a notable decrease of LC3B II/GAPDH ratio or Beclin-1 was observed in Br@MPMW treatment groups, which was consistent with our previous results. This might be due to a significant ROS inhibition effect by Br, which resulted in the inhibition of autophagy activity, to some extent.
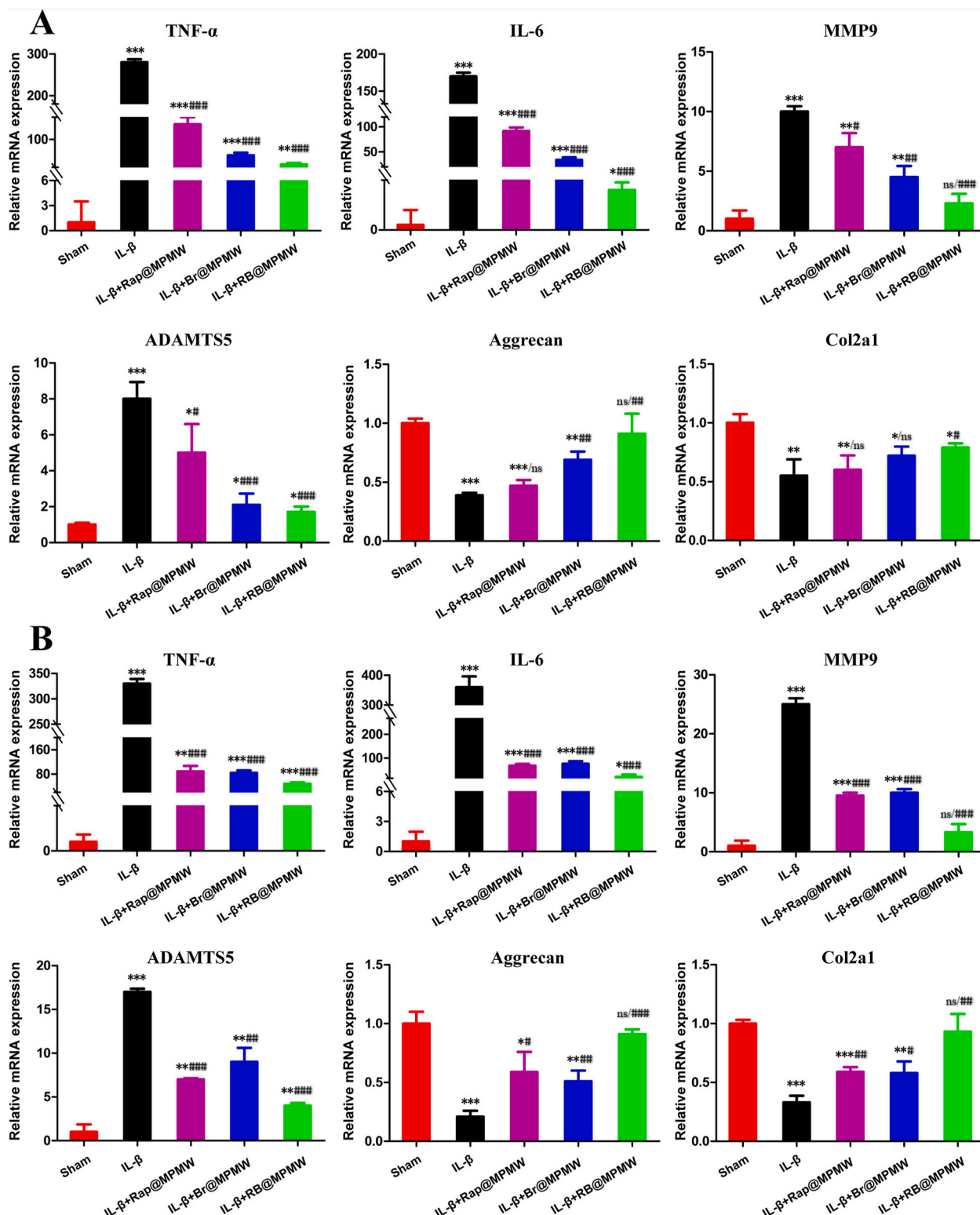
Fig. 5. The expression of OA-related genes (TNF-α, IL-6, MMP9, ADAMTS5, Aggrecan and Col2a1) after (A) 36 h and (B) 72 h treatment with different samples and further exposure to IL-1β (10 ng/mL). Data are shown as the means ± SD of triplicate independent experiments. *, # indicate p < 0.05; **, ## indicate p < 0.01; ***, ### indicate p < 0.001; ns indicates not significant. * indicates comparisons with the sham group and # indicates comparisons with the IL-1β treatment group.

On the other hand, loading with Rap rescued the inhibition of autophagy activity.

To comprehensively uncover the dynamic changes of intracellular oxidative stress and autophagy activity, we further detected autophagy and cellular ROS levels *in vitro* using a mixture of CYTO-ID, CellRox Green and Hoechst 33342 dyes. After ATDC5 cells incubated with IL-1β and RB@MPMW at different time points (0, 12, 24, 36, 48 and 72 h), the dyes mixture was applied to incubated with them for 15 min. The fluorescence images showed in Fig. 6B revealed a significant increase in intracellular ROS production after treatment for 12 h. However, a 24 h
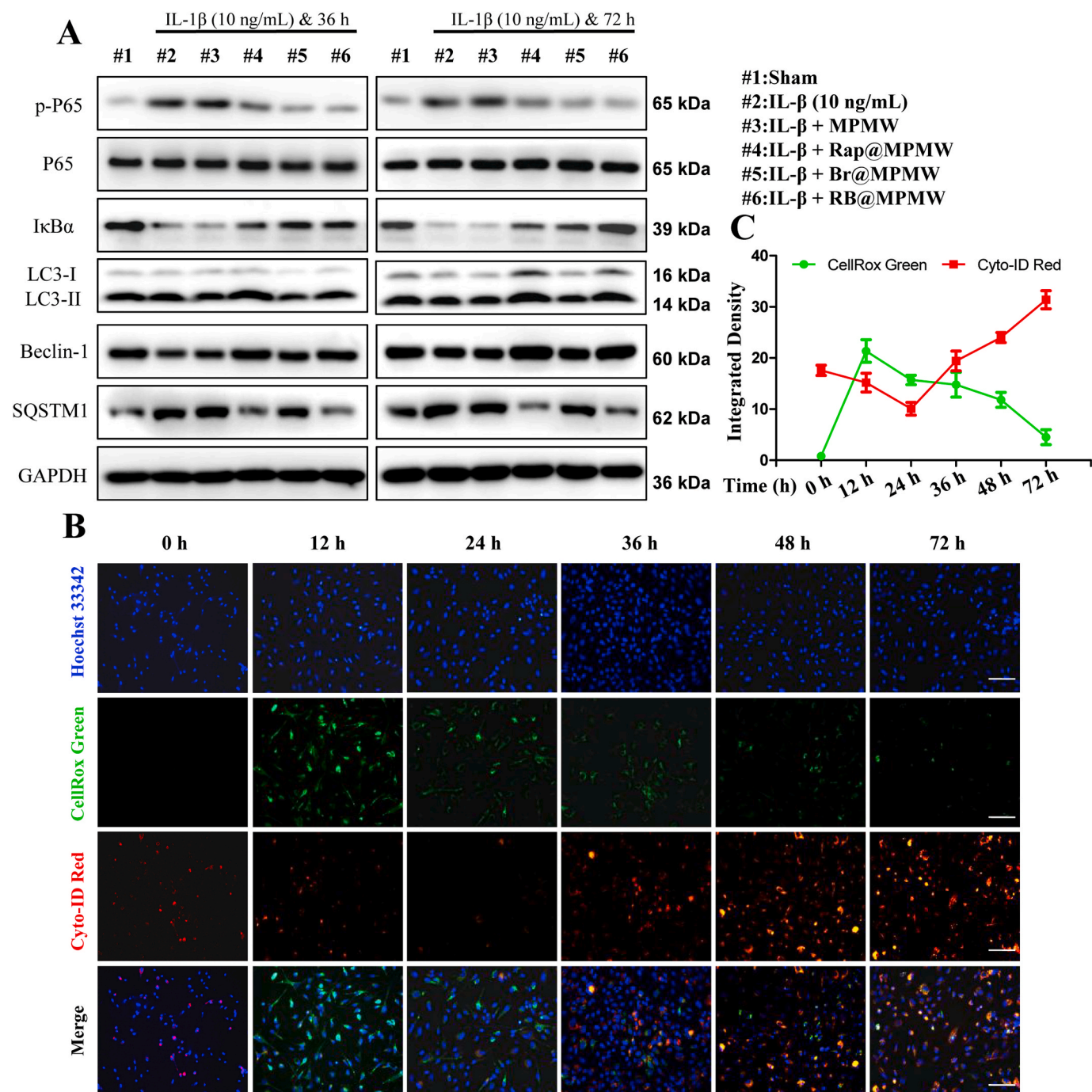
Fig. 6. (A) Some key proteins expression in autophagy and NF-κB signal pathway. (B) Fluorescence images of ATDC5 cells stained with Cyto-ID Red and CellRox Green after treated with RB@MPMW (50 μg/mL), IL-1β (10 ng/mL) and NIR laser (808 nm, 1 W/cm^2) for different incubation time (scale bar: 25 μm). (C) Quantitative analysis of dynamic changes of autophagy activity and ROS via calculating average intensity by ImageJ software.

co-culture with IL-1β and RB@MPMW resulted in a significant reduction in total cellular ROS level which might due to the superb anti-ROS effect of Br. Furthermore, we also observed a gradual decrease in intracellular ROS production from 24 h to 72 h. Autophagy activity was found at a low level after treatment for 24 h, contributing the rapid release of Br. However, cumulative release of Rap gradually activated autophagy activity from 24 h to 72 h. Therefore, the mutual complementary and well-designed therapeutic strategy further demonstrated the superiority of RB@MPMW.

In addition, the dynamic changes in autophagy activity and cellular ROS level were consistent with the results above (Fig. 6C). Overall, it was evident that RB@MPMW nanoparticles comprehensively

suppressed inflammation and exerted chondrocyte protective effects.

3.9. Rescue effect on mitochondrial function in chondrocytes

Several studies have reported that impairment of mitochondrial homeostasis in an overwhelming inflammatory microenvironment results in obstacles of cellular energy supply, and the impairment of mitochondrial homeostasis further accelerates chondrocyte apoptosis [57,58]. Previous studies have reported restoring the chondrocytes' mitochondrial dysfunction may be a possible way to rescue the apoptotic chondrocytes [59]. Other reports have also shown that bilirubin activates AMPK and promotes mitochondrial biosynthesis, thereby directly

increases the mitochondrial oxidative phosphorylation capacity and ATP production [60].

In this study, mitochondrial function of ATDC5 cells was determined *in vitro* following the treatment of IL-1β and various samples via OCR analysis. We found that 24-h treatment with IL-1β (10 ng/mL) resulted in the reduction of both basal and maximal respiration, indicating downregulation of mitochondrial function in chondrocytes (Fig. 7A and B). Additionally, we observed that ATP production and spare respiration capacity of the chondrocytes were also inhibited in IL-1β alone treatment group. However, treatment with Rap@MPMW, Br@MPMW and RB@MPMW gradually improved mitochondrial function and reprogrammed energy metabolism. More importantly, the Br@MPMW treatment group exhibited more powerful effect than the Rap@MPMW group. We further explored the effects of these samples on AMPK signaling pathway. Western blot results indicated RB@MPM continuously phosphorylated AMPK (p-AMPK) and sequentially activated the Sirtuin1 (SIRT1) as well as proliferator-activated receptor-γ coactivator-1α (PGC-1α). Furthermore, these drug-loaded samples rescued energy metabolism of chondrocytes following IL-1β stimulation and exerted protective effects on OA therapy (Fig. 7C–E). Although AMPK activation might further manipulate autophagy activity, our findings showed the responsive inhibition of autophagy played a dominant role when bilirubin was applied to scavenge oxygen free radicals.

3.10. Evaluation of MR/IVIS imaging properties of nanoparticles

As previously reported, MOF structure might endow the nanocarrier with superior MR imaging property [61,62]. Hence, the evaluation of MRI ability of as-prepared nanoparticles was performed *in vitro* and *in vivo*. As shown in Fig. 8A and B, it was measured that the relaxation rate values were 4.4593 and 5.7247 mm^{-1} s^{-1} for MPM and MPMW, respectively, indicating that both MPM and MPMW had concentration-dependent imaging effects and no significant difference on MRI performance. Further, MPM and MPMW solutions were respectively intra-articularly injected into ACLT rat models to explore the cartilage affinity of MPMW *in vivo* via MR imaging. The T1-weighted MR imaging signal on the cartilage surface was slightly enhanced in MPMW-treated group after 1 h treatment (Fig. 8C). However, a significantly higher T1-weighted MRI signal intensity was observed in MPMW than MPM treated group after 12 h treatment. These results indicated that MPMW had more excellent cartilage affinity properties. IVIS imaging was also utilized to detect the cartilage affinity properties of MPMW as shown in Fig. 8D. After 3 days of injection, the red fluorescence was disappeared in the group of Cy5-MPM, while it could be observed in the group of Cy5-MPMW. It was obviously that MPMW retained in the joint for a longer time compared with that of MPM and the red fluorescence could not be detected until 4 days after injection. After IA injection for 48 h, the difference in fluorescence intensity between the two groups began to be distinct. Therefore, we selected this time point for detecting the distribution of nanoparticles *in vivo*. According to the results illustrated in Fig. 8E, it was found that the fluorescence intensity in Cy5-MPMW treatment group was more concentrated in the distal femur and proximal tibia, intestine and spleen, suggesting the effective cartilage targeting ability of Cy5-MPMW. However, in the Cy5-MPM treatment group, there was more fluorescence in the liver, intestine, spleen and synovium (Fig. 8E and S5A), with relatively less fluorescence in cartilage.

3.11. Protective effect of nanoparticles against ACLT-induced cartilage destruction

ACLT rat model was established to validate protective effects of RB@MPMW on chondrocytes homeostasis *in vivo*. From the H&E and S/F staining, the overall structure of the knee joint as well as the loss of cartilage surface were displayed, respectively (Fig. 9A and B). Significantly higher degrees of cartilage destruction were observed in the ACLT

group compared with the sham group. However, treatment with Rap@MPMW, Br@MPMW and RB@MPMW all resulted in the decrease of cartilage damage to varying degrees. Based on histological analysis, the ACLT group recorded the highest OARSI score, whereas RB@MPMW treated group recorded the lowest OARSI score among the four ACLT treatment groups (Fig. 9D). Immunohistochemical analysis was further performed to evaluate the expression profiles of P65, LC3B and MMP9. The positive expression levels of P65 and MMP9 in ACLT group were the highest among five groups. However, following treatment with Rap@MPMW, Br@MPMW and RB@MPMW, this expression pattern was reversed at different level. Interestingly, LC3B, one the hallmark of autophagy, was downregulated in ACLT group. Nevertheless, treatment with Rap@MPMW and RB@MPMW resulted in a significant increase in LC3B expression (Fig. 9C and E). We also found a lower expression level of LC3B in Br@MPMW treatment group compared with the other groups, which was consistent with the western blot results *in vitro*. Over the course of experiments, there was no significant difference on the body weight among these groups (Fig. S5B). Furthermore, no significant systemic toxicity and important organs injury on rats after various samples administration were observed according to the results of some serological indicators and H&E staining (Fig. S5C and D). In addition, the detailed mechanism of dual-drug delivery nanoplatform described above with cartilage-targeting effect and NIR laser response for OA therapy was demonstrated in Fig. 10.

4. Discussion

To date, different cartilage-targeting nanoplatforms have been excavated and found to be crucial in overcoming dense type II collagen barriers as well as acting as effective drug carriers. For example, Bajpayee et al. demonstrated that DEX-loaded avidin aided rapid penetration into cartilage and therefore was an ideal IA treatment approach for OA, owing to the small size and positive charge characteristic of avidin [63]. On the other hand, chondrocyte-affinity peptide (DWRVIIPPRPSA) decorated PEGylated polyamidoamine was previously prepared and found to successfully penetrate into the cartilage [36]. This chondrocyte-affinity peptide has facilitated the longer residence time of nanoparticles in cartilage and was therefore a perfect modification of nanocarrier for OA therapy. In this study, we synthesized RB@MPMW that possessed numerous excellent characteristics, including a small diameter, a positive potential and ideal cartilage affinity ability, which were ideal for overcoming the dense type II collagen barrier and effectively exerting precise therapeutic effects against OA. Interestingly, from our experimental results, peptide-modified drug-loaded nanocarrier is more easily to approach to the chondrocytes which are mainly lying in the cartilage lacuna, and further engulfed by these cells. The confocal laser scanning results shown in Fig. 3A demonstrated that our nanocarriers didn't enter into the nucleus and most of them were resided in the cytoplasm, further indicating these two agents mainly functioning in cytoplasm. In addition, according to the results shown in Fig. S6, these nanoparticles were trafficked preferentially into lysosomes in the first 4 h. However, according to previous studies [48,64], MOF structure could be well degraded in the acidic microenvironment like lysosomes compared with other subcellular organelles of chondrocyte whose pH were at neutral. Since this acidic microenvironment does not significantly affect the efficacy of rapamycin [65] and bilirubin [66,67] which might further transport to the cytoplasm, RB@MPMW taken up by chondrocytes lysosomes may be more conducive to the possible degradation of MOF structure and the effective release of the drugs, further reflecting the advantages of our nanocarrier, to a certain extent.

Numerous studies have implied the significance of integrating anti-ROS effect and promoting autophagy activity in OA treatment [68,69]. Firstly, the disruption of anti-oxidative system in chondrocytes may activate many crucial transcriptional factors including NF-κB and further initiate the expression of multiple inflammatory factors and downstream matrix-degrading proteases [70]. These alterations could
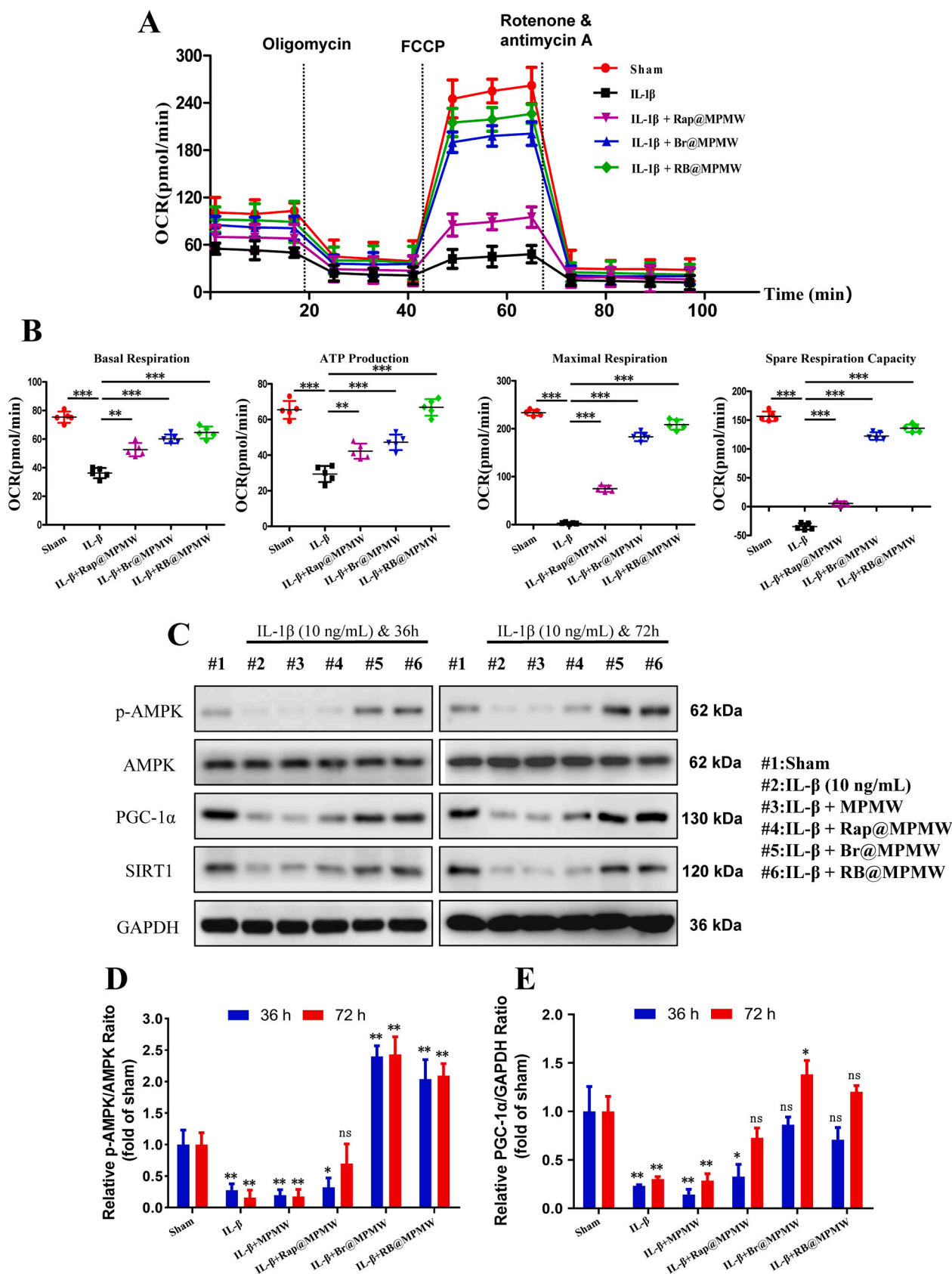
Fig. 7. (A) OCR of ATDC5 cells after different treatments. (B) Some parameters were shown based on the OCR analysis, including basal respiration, ATP production, maximal respiration and spare respiration capacity. (C) The effects of various treatments on the AMPK-SIRT1-PGC-1α signaling pathway were determined. (D,E) The relative expression of p-AMPK/AMPK and PGC-1α/GAPDH among various groups (compared with the sham group). * indicates $p < 0.05$; ** indicates $p < 0.01$; *** indicates $p < 0.001$; ^{ns} indicates not significant.
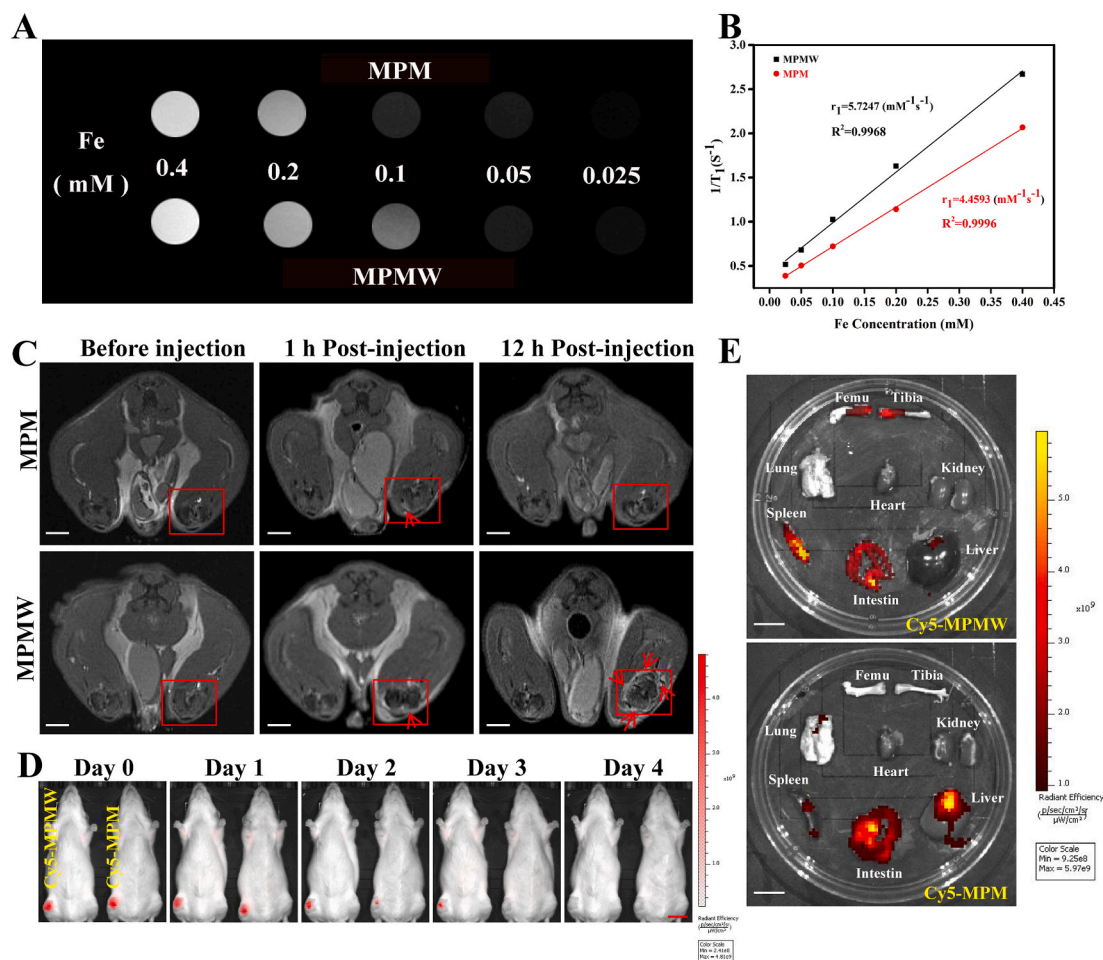
Fig. 8. (A) The T1-weight MR images of MPM & MPMW with different Fe concentrations (0.025, 0.05, 0.1, 0.2 and 0.4 mM) *in vitro*. (B) The respective r1 relaxivity curves of MPM & MPMW. (C) The T1-weight MR images of ACLT rat model intra-articularly treated with MPM & MPMW (50 μg/mL, 20 μL) for indicated time points (scale bar: 0.5 cm). The red box shows the image of the right knee joint before and after the injection of MPM & MPMW, while the arrow mainly shows the signal enhancement area of the cartilage before and after the injection. (D) The IVIS images of ACLT rat model after IA injection of MPM & MPMW (50 μg/mL, 20 μL) for indicated time points (scale bar: 2 cm). (E) The IVIS images of some important organs to show the retention of nanoparticles at 48 h after IA injection (scale bar: 2 cm).

further result in cell senescence and apoptosis. Therefore, early application of agents that effectively scavenge ROS might be an important approach for suppressing degeneration of cartilage. Herein, bilirubin was loaded into multifunctional nanocarrier for scavenging oxygen free radicals and further exerted anti-inflammatory effect at cellular level. Similarly, Yao and co-workers found Br-loaded silk fibrin nanoparticles exhibited superb therapeutic effects against acute pancreatitis [10], particularly because Br inhibited the NF-κB but activated the Nrf2/HO-1 signaling pathways. On the other hand, autophagy is a self-protective process that also exerts favorable effects on chondrocytes against some detrimental stresses and rescues chondrocytes from apoptosis. Rapamycin, an activator of autophagy, has been reported to restore osteogenic differentiation ability successfully in bone marrow-derived mesenchymal stem cells (BMSCs) and partially promoted fracture healing [71]. In addition, Rap was demonstrated to be feasible for the treatment of post-traumatic OA (PTOA). Matsuzaki et al. previously found that Rap-incorporated gelatin hydrogel micelles effectively prevented pathological development of OA *in vivo* [19]. However, our results also indicated that combining the potent anti-ROS agent bilirubin and autophagy-activating agent rapamycin generated synergistic and complementary protective effects on cartilage.

Intriguingly, we found Br@MPMW exerted superb anti-ROS effect in chondrocytes but blocked autophagy flux, possibly due to the rapid elimination of cellular ROS level, which subsequently leading to a gradual decrease of autophagy activity. Based on these findings, we designed NIR laser-triggered Rap accelerated release manner when the released bilirubin scavenged much free radicals and inhibited autophagy activity.

Numerous studies have also reported that dual-drug loaded nanocarriers hold great promise for OA therapy. For example, Kang et al. synthesized novel dual drug-loaded nanopartilces, with rapid release of diclofenac against inflammation and kartogenin-controlled release for cartilage regeneration, demonstrating a remarkable efficacy [72]. What's more, in our study, it showed the photothermal effect could promote the release of two drugs. Similarly, as previously reported, the local temperature increment caused by photothermal effect and the drugs' efficacy could have a synergistic good effect on arthritis treatment [73].

Mitochondrial homeostasis is often impaired in the inflammatory microenvironment, and the excessive ROS production may cause irreversible damage to mitochondrial DNA (mt DNA), which may block energy supply and further accelerate apoptosis of chondrocytes [70,74, 75]. Previous studies have shown that bilirubin might act as an effective AMPK activator, thereby regulate energy metabolism [60]. Our results further confirmed that Br incorporated nanocarriers, including Br@MPMW and RB@MPMW, continuously phosphorylated AMPK and activated the AMPK-SIRT1-PGC-1α signaling pathway after IL-1β stimulation and exerted protective effects that were vital during OA therapy.
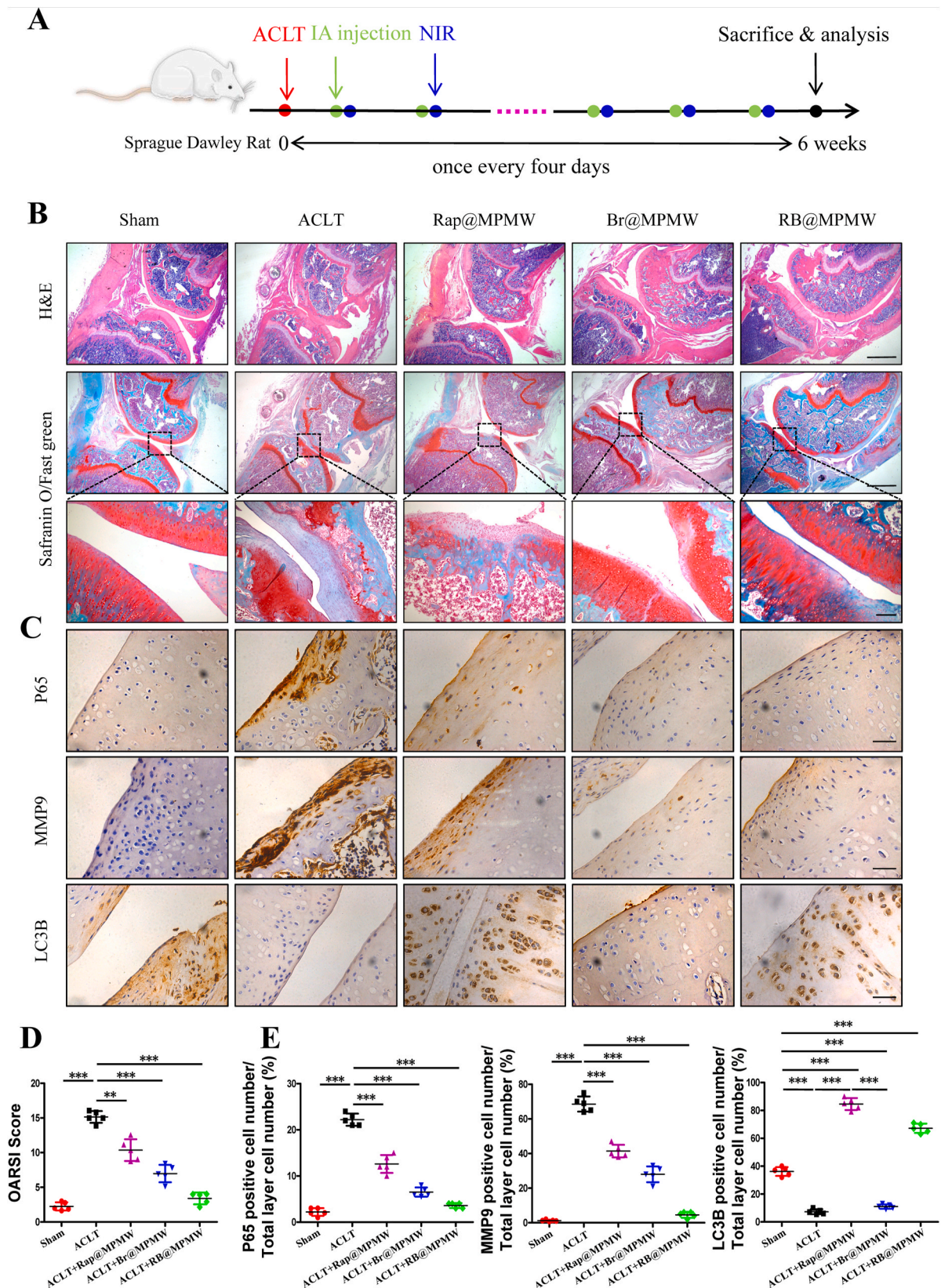
Fig. 9. (A) Treatment schedule. (B) H&E staining and Safranin O/Fast green staining of the articular cartilage after 6 weeks treatment with different samples (scale bar: top and center, 450 μm; bottom, 150 μm). (C) Immunohistochemisy analysis of the articular cartilage after 6 weeks treatment with different samples (n = 5, scale bar: 45 μm). (D) The overall OARSI scores of the articular cartilage. (E) Relative expression of P65, MMP9 and LC3B for each group. ** indicate p < 0.01; *** indicate p < 0.001.
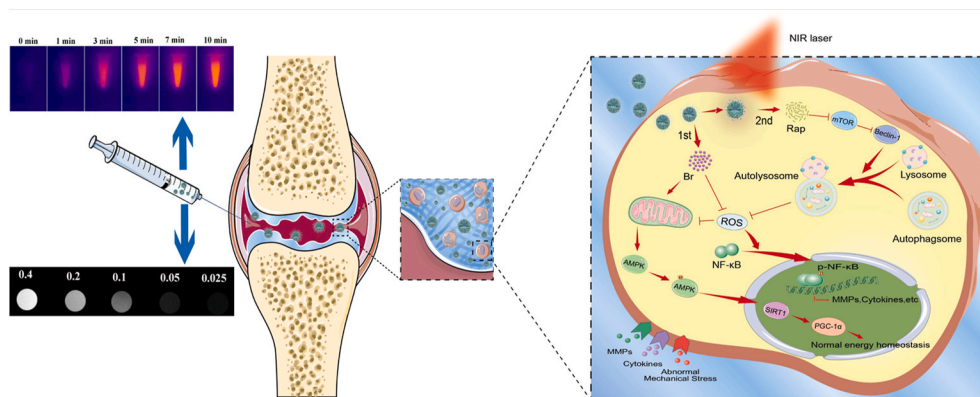
Fig. 10. The mechanism of dual-drug delivery nanoplatform with cartilage-targeting effect and NIR laser response for OA therapy.

Taken together, these findings of this study demonstrated cartilage-targeting peptide-modified dual-drug loaded nanoparticles with NIR laser-stimulated sequential release of agents synergistically scavenged cellular ROS and enhanced autophagy activity. Functionally, the dual-drug delivery system promoted mitochondrial energy metabolism and delayed cartilage degeneration in ACLT rat model.

However, in our study, we merely conducted young rats OA model which might be a weakness to the *in vivo* efficacy work. The efficacy will be investigated on older rats OA model in our further experiments. As for the clinical application, although NIR irradiation could be implemented in hospital or at home with a portable device after IA injection, there are many concerns need to be clearly verified by lots of experiments including the injection volume of nanoparticles, the power and time of the NIR irradiation and so on. Overall, our findings provide a new dual drug-loaded nanocarrier that may hold promise for OA treatment.

5. Conclusions

In this study, we successfully synthesized a novel dual-drug delivery nanoplatform (RB@MPMW) for OA therapy. Experimental results indicated that the dual-drug delivery system, with excellent NIR laser-stimulated responsive drug release effect, could sequentially realize scavenging cellular free radicals by Br and enhancing autophagy activity via Rap. Moreover, RB@MPMW specifically targeted the cartilage with the help of WYRGRL and positive surface potential, and possessed outstanding MR imaging properties to monitor its therapeutic effects *in vivo*. Importantly, the nanoplatform enhanced energy metabolism of chondrocytes via activating the AMPK-SIRT1-PGC-1α signaling pathway, further rescued cell apoptosis *in vitro* and repressed cartilage degeneration *in vivo*. Taken together, the developed multifunctional nanoplatform pave a new avenue for OA therapy.

CRediT author contribution statement

Song Xue: Investigation, Methodology, Data curation, Formal analysis, Writing - original draft. **Xiaojun Zhou:** Investigation, Methodology, Data curation, Formal analysis, Funding acquisition, Funding acquisition. **Weilin Sang:** Funding acquisition, Data curation, Visualization, Formal analysis. **Cong Wang:** Investigation, Formal analysis, Resources. **Haiming Lu:** Formal analysis, Funding acquisition. **Yiming Xu:** Resources. **Yiming Zhong:** Data curation. **Libo Zhu:** Investigation, Formal analysis, Funding acquisition. **Chuanglong He:** Conceptualization, Supervision, Writing - review & editing, Project administration, Funding acquisition. **Jinzhong Ma:** Funding acquisition, Conceptualization, Supervision, Writing - review & editing, Project administration.

Declaration of competing interest

All authors declared that no conflict interest existed.

Acknowledgements

Appendix A. Supplementary data

Supplementary data to this article can be found online at https://doi.org/10.1016/j.bioactmat.2021.01.017.

References

[1] M. Kloppenburg, F. Berenbaum, Osteoarthritis year in review 2019: epidemiology and therapy, Osteoarthritis Cartilage 28 (2020) 242–248.
[2] N. Nasiri, S. Hosseini, M. Alini, A. Khademhosseini, M. Baghaban Eslaminejad, Targeted cell delivery for articular cartilage regeneration and osteoarthritis treatment, Drug Discov, Today Off. 24 (2019) 2212–2224.
[3] L. Fraenkel, E. Buta, L. Suter, M. Dubreuil, C. Levy, C. Najem, M. Brennan, B. Corn, R. Kerns, J. Goulet, Nonsteroidal anti-inflammatory drugs vs cognitive behavioral therapy for arthritis pain: a randomized withdrawal trial, JAMA Intern. Med. (2020), e202821.
[4] B.R. da Costa, S. Reichenbach, N. Keller, L. Nartey, S. Wandel, P. Juni, S. Trelle, Effectiveness of non-steroidal anti-inflammatory drugs for the treatment of pain in knee and hip osteoarthritis: a network meta-analysis, Lancet 390 (2017) e21–e33.
[5] P. Lepetsos, A.G. Papavassiliou, ROS/oxidative stress signaling in osteoarthritis, Biochim. Biophys. Acta 1862 (2016) 576–591.
[6] M. Arra, G. Swarnkar, K. Ke, J.E. Otero, J. Ying, X. Duan, T. Maruyama, M.F. Rai, R. J. O'Keefe, G. Mbalaviele, J. Shen, Y. Abu-Amer, LDHA-mediated ROS generation in chondrocytes is a potential therapeutic target for osteoarthritis, Nat. Commun. 11 (2020) 3427.
[7] N. Dalbeth, K. Billington, A. Doyle, C. Frampton, P. Tan, O. Aati, J. Allan, J. Drake, A. Horne, L.K. Stamp, Effects of allopurinol dose escalation on bone erosion and urate volume in gout: a dual-energy computed tomography imaging study within a randomized, controlled trial, Arthritis Rheum. 71 (2019) 1739–1746.
[8] J. Yeo, Y.M. Lee, J. Lee, D. Park, K. Kim, J. Kim, J. Park, W.J. Kim, Nitric oxide-scavenging nanogel for treating rheumatoid arthritis, Nano Lett. 19 (2019) 6716–6724.
[9] G. Idelman, D.L.H. Smith, S.D. Zucker, Bilirubin inhibits the up-regulation of inducible nitric oxide synthase by scavenging reactive oxygen species generated by the toll-like receptor 4-dependent activation of NADPH oxidase, Redox. Biol. 5 (2015) 398–408.
[10] Q. Yao, X. Jiang, Y.Y. Zhai, L.Z. Luo, H.L. Xu, J. Xiao, L. Kou, Y.Z. Zhao, Protective effects and mechanisms of bilirubin nanomedicine against acute pancreatitis, J. Contr. Release 322 (2020) 312–325.
[11] D.E. Kim, Y. Lee, M. Kim, S. Lee, S. Jon, S.H. Lee, Bilirubin nanoparticles ameliorate allergic lung inflammation in a mouse model of asthma, Biomaterials 140 (2017) 37–44.

[12] J.Y. Kim, D.Y. Lee, S. Kang, W. Miao, H. Kim, Y. Lee, S. Jon, Bilirubin nanoparticle preconditioning protects against hepatic ischemia-reperfusion injury, Biomaterials 133 (2017) 1–10.

[13] M.J. Kim, Y. Lee, S. Jon, D.Y. Lee, PEGylated bilirubin nanoparticle as an anti-oxidative and anti-inflammatory demulcent in pancreatic islet xenotransplantation, Biomaterials 133 (2017) 242–252.

[14] D.Y. Lee, S. Kang, Y. Lee, J.Y. Kim, D. Yoo, W. Jung, S. Lee, Y.Y. Jeong, K. Lee, S. Jon, PEGylated bilirubin-coated iron oxide nanoparticles as a biosensor for magnetic relaxation switching-based ROS detection in whole blood, Theranostics 10 (2020) 1997–2007.

[15] Y. Lee, K. Sugihara, M.G. Gillilland 3rd, S. Jon, N. Kamada, J.J. Moon, Hyaluronic acid-bilirubin nanomedicine for targeted modulation of dysregulated intestinal barrier, microbiome and immune responses in colitis, Nat. Mater. 19 (2020) 118–126.

[16] Y. Lee, H. Kim, S. Kang, J. Lee, J. Park, S. Jon, Bilirubin nanoparticles as a nanomedicine for anti-inflammation therapy, Angew Chem. Int. Ed. Engl. 55 (2016) 7460–7463.

[17] W.S. Lian, J.Y. Ko, R.W. Wu, Y.C. Sun, Y.S. Chen, S.L. Wu, L.H. Weng, H. Jahr, F. S. Wang, MicroRNA-128a represses chondrocyte autophagy and exacerbates knee osteoarthritis by disrupting Atg12, Cell Death Dis. 9 (2018) 919.

[18] J.H. Duarte, Osteoarthritis: autophagy prevents age-related OA, Nat. Rev. Rheumatol. 11 (2015) 683.

[19] T. Matsuzaki, T. Matsushita, Y. Tabata, T. Saito, T. Matsumoto, K. Nagai, R. Kuroda, M. Kurosaka, Intra-articular administration of gelatin hydrogels incorporating rapamycin-micelles reduces the development of experimental osteoarthritis in a murine model, Biomaterials 35 (2014) 9904–9911.

[20] G. Jones, T. Winzenberg, Osteoarthritis: a new short-term treatment option? Lancet 394 (2019) 1967–1968.

[21] I.A. Jones, R. Togashi, M.L. Wilson, N. Heckmann, C.T. Vangsness Jr., Intra-articular treatment options for knee osteoarthritis, Nat. Rev. Rheumatol. 15 (2019) 77–90.

[22] D. Agas, F. Laus, G. Lacava, A. Marchegiani, S. Deng, F. Magnoni, G.G. Silva, P. Di Martino, M.G. Sabbieti, R. Censi, Thermosensitive hybrid hyaluronan/p(HPMAm-lac)-PEG hydrogels enhance cartilage regeneration in a mouse model of osteoarthritis, J. Cell. Physiol. 234 (2019) 20013–20027.

[23] X. Chen, Y. Liu, Y. Wen, Q. Yu, J. Liu, Y. Zhao, J. Liu, G. Ye, A photothermal-triggered nitric oxide nanogenerator combined with siRNA for precise therapy of osteoarthritis by suppressing macrophage inflammation, Nanoscale 11 (2019) 6693–6709.

[24] Y. Zhao, C. Wei, X. Chen, J. Liu, Q. Yu, Y. Liu, J. Liu, Drug delivery system based on near-infrared light-responsive molybdenum disulfide nanosheets controls the high-efficiency release of dexamethasone to inhibit inflammation and treat osteoarthritis, ACS Appl. Mater. Interfaces 11 (2019) 11587–11601.

[25] W. Cheng, X. Zeng, H. Chen, Z. Li, W. Zeng, L. Mei, Y. Zhao, Versatile polydopamine platforms: synthesis and promising applications for surface modification and advanced nanomedicine, ACS Nano 13 (2019) 8537–8565.

[26] Q. Lin, Y. Yang, Y. Ma, R. Zhang, J. Wang, X. Chen, Z. Shao, Bandgap engineered polypyrrole-polydopamine hybrid with intrinsic Raman and photoacoustic imaging contrasts, Nano Lett. 18 (2018) 7485–7493.

[27] L. Ao, C. Wu, K. Liu, W. Wang, L. Fang, L. Huang, W. Su, Polydopamine-derived hierarchical nanoplatforms for efficient dual-modal imaging-guided combination in vivo cancer therapy, ACS Appl. Mater. Interfaces 10 (2018) 12544–12552.

[28] Y. Cen, W.J. Deng, Y. Yang, R.Q. Yu, X. Chu, Core-shell-shell multifunctional nanoplatform for intracellular tumor-related mRNAs imaging and near-infrared light triggered photodynamic-photothermal synergistic therapy, Anal. Chem. 89 (2017) 10321–10328.

[29] Y. Lu, L. Li, Z. Lin, L. Wang, L. Lin, M. Li, Y. Zhang, Q. Yin, Q. Li, H. Xia, A new treatment modality for rheumatoid arthritis: combined photothermal and photodynamic therapy using Cu(7.2) S(4) nanoparticles, Adv. Healthc. Mater. 7 (2018), e1800013.

[30] Z. Ouyang, T. Tan, C. Liu, J. Duan, W. Wang, X. Guo, Q. Zhang, Z. Li, Q. Huang, P. Dou, T. Liu, Targeted delivery of hesperetin to cartilage attenuates osteoarthritis by bimodal imaging with Gd2(CO3)3@PDA nanoparticles via TLR-2/NF-kappaB/Akt signaling, Biomaterials 205 (2019) 50–63.

[31] Z. Wang, L. Wang, N. Prabhakar, Y. Xing, J.M. Rosenholm, J. Zhang, K. Cai, CaP coated mesoporous polydopamine nanoparticles with responsive membrane permeation ability for combined photothermal and siRNA therapy, Acta Biomater. 86 (2019) 416–428.

[32] Y. Xing, J. Zhang, F. Chen, J. Liu, K. Cai, Mesoporous polydopamine nanoparticles with co-delivery function for overcoming multidrug resistance via synergistic chemo-photothermal therapy, Nanoscale 9 (2017) 8781–8790.

[33] Y. Chen, X. Feng, Y. Zhao, X. Zhao, X. Zhang, Mussel-inspired polydopamine coating enhances the intracutaneous drug delivery from nanostructured lipid carriers dependently on a follicular pathway, Mol. Pharm. 17 (2020) 1215–1225.

[34] J. Hu, Q. Wang, Y. Wang, G. You, P. Li, L. Zhao, H. Zhou, Polydopamine-based surface modification of hemoglobin particles for stability enhancement of oxygen carriers, J. Colloid Interface Sci. 571 (2020) 326–336.

[35] S. Yan, Q. Huang, J. Chen, X. Song, Z. Chen, M. Huang, P. Xu, J. Zhang, Tumor-targeting photodynamic therapy based on folate-modified polydopamine nanoparticles, Int. J. Nanomed. 14 (2019) 6799–6812.

[36] Q. Hu, Q. Chen, X. Yan, B. Ding, D. Chen, L. Cheng, Chondrocyte affinity peptide modified PAMAM conjugate as a nanoplatform for targeting and retention in cartilage, Nanomedicine 13 (2018) 749–767.

[37] H. Chen, Z. Qin, J. Zhao, Y. He, E. Ren, Y. Zhu, G. Liu, C. Mao, L. Zheng, Cartilage-targeting and dual MMP-13/pH responsive theranostic nanoprobes for osteoarthritis imaging and precision therapy, Biomaterials 225 (2019) 119520.

[38] D.A. Rothenfluh, H. Bermudez, C.P. O'Neil, J.A. Hubbell, Biofunctional polymer nanoparticles for intra-articular targeting and retention in cartilage, Nat. Mater. 7 (2008) 248–254.

[39] H. Okada, S. Itoh, K. Nii, M. Sugino, N. Fuke, K. Koyano, S. Yasuda, T. Kusaka, Bilirubin photoisomers in rhesus monkey serum, J. Photochem. Photobiol., B 185 (2018) 50–54.

[40] D.W. Holt, T. Lee, A. Johnston, Measurement of sirolimus in whole blood using high-performance liquid chromatography with ultraviolet detection, Clin. Therapeut. 22 (Suppl. B) (2000) B38–48.

[41] W. Feng, W. Nie, C. He, X. Zhou, L. Chen, K. Qiu, W. Wang, Z. Yin, Effect of pH-responsive alginate/chitosan multilayers coating on delivery efficiency, cellular uptake and biodistribution of mesoporous silica nanoparticles based nanocarriers, ACS Appl. Mater. Interfaces 6 (2014) 8447–8460.

[42] S. Xue, Q. Shao, L.B. Zhu, Y.F. Jiang, C. Wang, B. Xue, H.M. Lu, W.L. Sang, J.Z. Ma, LDC000067 suppresses RANKL-induced osteoclastogenesis in vitro and prevents LPS-induced osteolysis in vivo, Int. Immunopharm. 75 (2019) 105826.

[43] F. Zhou, J. Mei, S. Yang, X. Han, H. Li, Z. Yu, H. Qiao, T. Tang, Modified ZIF-8 nanoparticles attenuate osteoarthritis by reprogramming the metabolic pathway of synovial macrophages, ACS Appl. Mater. Interfaces 12 (2020) 2009–2022.

[44] Y. Jiang, L. Zhu, T. Zhang, H. Lu, C. Wang, B. Xue, X. Xu, Y. Liu, Z. Cai, W. Sang, Y. Hua, J. Ma, BRD4 has dual effects on the HMGB1 and NF-κB signalling pathways and is a potential therapeutic target for osteoarthritis, Biochim. Biophys. Acta (BBA) - Mol. Basis Dis. 1863 (2017) 3001–3015.

[45] Y. Jiang, W. Sang, C. Wang, H. Lu, T. Zhang, Z. Wang, Y. Liu, B. Xue, S. Xue, Z. Cai, Y. Hua, L. Zhu, J. Ma, Oxymatrine exerts protective effects on osteoarthritis via modulating chondrocyte homoeostasis and suppressing osteoclastogenesis, J. Cell. Mol. Med. 22 (2018) 3941–3954.

[46] F. Lu, S.H. Wu, Y. Hung, C.Y. Mou, Size effect on cell uptake in well-suspended, uniform mesoporous silica nanoparticles, Small 5 (2009) 1408–1413.

[47] S. Lu, W. Hu, Z. Zhang, Z. Ji, T. Zhang, Sirolimus-coated, poly(L-lactic acid)-modified polypropylene mesh with minimal intra-peritoneal adhesion formation in a rat model, Hernia 22 (2018) 1051–1060.

[48] C. Zhang, S. Hong, M.D. Liu, W.Y. Yu, M.K. Zhang, L. Zhang, X. Zeng, X.Z. Zhang, pH-sensitive MOF integrated with glucose oxidase for glucose-responsive insulin delivery, J. Contr. Release 320 (2020) 159–167.

[49] L. Zhang, Y. Gao, S. Sun, Z. Li, A. Wu, L. Zeng, pH-Responsive metal-organic framework encapsulated gold nanoclusters with modulated release to enhance photodynamic therapy/chemotherapy in breast cancer, J. Mater. Chem. B. 8 (2020) 1739–1747.

[50] F. Xiong, Z. Qin, H. Chen, Q. Lan, Z. Wang, N. Lan, Y. Yang, L. Zheng, J. Zhao, D. Kai, pH-responsive and hyaluronic acid-functionalized metal-organic frameworks for therapy of osteoarthritis, J. Nanobiotechnol. 18 (2020) 139.

[51] R. Giordo, G.K. Nasrallah, O. Al-Jamal, P. Paliogiannis, G. Pintus, Resveratrol inhibits oxidative stress and prevents mitochondrial damage induced by zinc oxide nanoparticles in zebrafish (Danio rerio), Int. J. Mol. Sci. 21 (2020) 3838.

[52] Y. Gu, K. Ren, C. Jiang, L. Wang, Q. Yao, Regulation of cartilage damage caused by lack of Klotho with thioredoxin/peroxiredoxin (Trx/Prx) system and succedent NLRP3 activation in osteoarthritis mice, Am. J. Transl. Res. 11 (2019) 7338–7350.

[53] S.W. Tsai, C.C. Lin, S.C. Lin, S.P. Wang, D.H. Yang, Isorhamnetin ameliorates inflammatory responses and articular cartilage damage in the rats of monosodium iodoacetate-induced osteoarthritis, Immunopharmacol. Immunotoxicol. 41 (2019) 504–512.

[54] N. Ahmad, M.Y. Ansari, S. Bano, T.M. Haqqi, Imperatorin suppresses IL-1β-induced iNOS expression via inhibiting ERK-MAPK/AP1 signaling in primary human OA chondrocytes, Int. Immunopharm. 85 (2020) 106612.

[55] Q. Shao, S. Xue, Y. Jiang, H. Lu, W. Sang, C. Wang, B. Xue, Y. Liu, L. Zhu, J. Ma, Esculentoside A protects against osteoarthritis by ameliorating inflammation and repressing osteoclastogenesis, Int. Immunopharm. 82 (2020) 106376.

[56] D.J. Klionsky, F.C. Abdalla, H. Abeliovich, R.T. Abraham, A. Acevedo-Arozena, K. Adeli, I. Agholme, M. Agnello, P. Agostinis, J.A. Aguirre-Ghiso in, et al., Guidelines for the use and interpretation of assays for monitoring autophagy, Autophagy 8 (2012) 445–544.

[57] O. Alvarez-Garcia, T. Matsuzaki, M. Olmer, L. Plate, J.W. Kelly, M.K. Lotz, Regulated in development and DNA damage response 1 deficiency impairs autophagy and mitochondrial biogenesis in articular cartilage and increases the severity of experimental osteoarthritis, Arthritis Rheum. 69 (2017) 1418–1428.

[58] S. Farnaghi, I. Prasadam, G. Cai, T. Friis, Z. Du, R. Crawford, X. Mao, Y. Xiao, Protective effects of mitochondria-targeted antioxidants and statins on cholesterol-induced osteoarthritis, Faseb. J. 31 (2017) 356–367.

[59] R.S. Lane, Y. Fu, S. Matsuzaki, M. Kinter, K.M. Humphries, T.M. Griffin, Mitochondrial respiration and redox coupling in articular chondrocytes, Arthritis Res. Ther. 17 (2015) 54.

[60] L. Vítek, Bilirubin as a signaling molecule, Med. Res. Rev. 40 (2020) 1335–1351.

[61] R.A. Hamideh, B. Akbari, P. Fathi, S.K. Misra, A. Sutrisno, F. Lam, D. Pan, Biodegradable MRI visible drug eluting stent reinforced by metal organic frameworks, Adv. Healthc. Mater. 9 (14) (2020), e2000136.

[62] L. Chen, J. Zhang, X. Zhou, S. Yang, Q. Zhang, W. Wang, Z. You, C. Peng, C. He, Merging metal organic framework with hollow organosilica nanoparticles as a versatile nanoplatform for cancer theranostics, Acta Biomater. 86 (2019) 406–415.

[63] A.G. Bajpayee, R.E. De la Vega, M. Scheu, N.H. Varady, I.A. Yannatos, L.A. Brown, Y. Krishnan, T.J. Fitzsimons, P. Bhattacharya, E.H. Frank, A.J. Grodzinsky, R. M. Porter, Sustained intra-cartilage delivery of low dose dexamethasone using a cationic carrier for treatment of post traumatic osteoarthritis, Eur. Cell. Mater. 34 (2017) 341–364.

[64] Q. Xing, Y. Pan, Y. Hu, L. Wang, Review of the biomolecular modification of the metal-organ-framework, Front. Chem. 8 (2020) 642.

[65] P. Liu, X. Liu, Y. Cheng, S. Zhong, X. Shi, S. Wang, M. Liu, J. Ding, W. Zhou, Core-shell nanosystems for self-activated drug-gene combinations against triple-negative breast cancer, ACS Appl. Mater. Interfaces 12 (2020) 53654–53664.

[66] W.K. Kauer, P. Burdiles, A.P. Ireland, G.W. Clark, J.H. Peters, C.G. Bremner, T. R. DeMeester, Does duodenal juice reflux into the esophagus of patients with complicated GERD? Evaluation of a fiberoptic sensor for bilirubin, Am. J. Surg. 169 (1995) 98–103, discussion 103-104.

[67] R. Cuomo, G. Koek, D. Sifrim, J. Janssens, J. Tack, Analysis of ambulatory duodenogastroesophageal reflux monitoring, Dig. Dis. Sci. 45 (2000) 2463–2469.

[68] G. Zhong, X. Yang, X. Jiang, A. Kumar, H. Long, J. Xie, L. Zheng, J. Zhao, Dopamine-melanin nanoparticles scavenge reactive oxygen and nitrogen species and activate autophagy for osteoarthritis therapy, Nanoscale 11 (2019) 11605–11616.

[69] S. Portal-Núñez, P. Esbrit, M.J. Alcaraz, R. Largo, Oxidative stress, autophagy, epigenetic changes and regulation by miRNAs as potential therapeutic targets in osteoarthritis, Biochem. Pharmacol. 108 (2016) 1–10.

[70] K.N. Reed, G. Wilson, A. Pearsall, V.I. Grishko, The role of mitochondrial reactive oxygen species in cartilage matrix destruction, Mol. Cell. Biochem. 397 (2014) 195–201.

[71] G.E. Yang, X. Duan, D. Lin, T. Li, D. Luo, L. Wang, K. Lian, Rapamycin-induced autophagy activity promotes bone fracture healing in rats, Exp. Ther. Med. 10 (2015) 1327–1333.

[72] M.L. Kang, J.E. Kim, G.I. Im, Thermoresponsive nanospheres with independent dual drug release profiles for the treatment of osteoarthritis, Acta Biomater. 39 (2016) 65–78.

[73] X. Zhang, X. Zhang, X. Wang, T. Wang, B. Bai, N. Zhang, Y. Zhao, Y. Yu, B. Wang, Efficient delivery of triptolide plus a miR-30-5p inhibitor through the use of near infrared laser responsive or CADY modified MSNs for efficacy in rheumatoid arthritis therapeutics, Front. Bioeng. Biotechnol. 8 (2020) 170.

[74] Y. Ding, Y. Zheng, J. Huang, W. Peng, X. Chen, X. Kang, Q. Zeng, UCP2 ameliorates mitochondrial dysfunction, inflammation, and oxidative stress in lipopolysaccharide-induced acute kidney injury, Int. Immunopharm. 71 (2019) 336–349.

[75] N.M. Khan, I. Ahmad, T.M. Haqqi, Nrf2/ARE pathway attenuates oxidative and apoptotic response in human osteoarthritis chondrocytes by activating ERK1/2/ELK1-P70S6K-P90RSK signaling axis, Free Radic. Biol. Med. 116 (2018) 159–171.